Progress in Natural Science: Materials International 36 (2026) 152–167

HOSTED BY

Contents lists available at ScienceDirect

Progress in Natural Science: Materials International

journal homepage: www.elsevier.com/locate/pnsmi

Preparation of pH-stable and ion-resistant mixed-graft ion exchange resins for efficient Nitrate Removal: Performance and mechanism

Yiming Zong[a,c], Wenjiao Ke[b], Yang Xue[b], Rui Xiao[a], Sixi Zhu[a], Shuya Zheng[a], Yongen Shi[a], Li Feng[a,c,*], Xuefeng Ren[a,**]

[a] State Key Laboratory of Coking Coal Resources Green Exploitation, China University of Mining and Technology, Xuzhou, 221008, China
[b] China Water Investment Co., LTD., Beijing 100053, China
[c] School of Chemical Engineering, China University of Mining and Technology, Xuzhou, 221008, China

ARTICLE INFO

Keywords:
Magnetic acrylic anion exchange resin
Quaternary ammonium group
Nitrate
γ-Fe2O3
Adsorption

ABSTRACT

Nitrate (NO_3^-) is a pervasive pollutant in industrial water treatment due to its widespread presence in industrial processes. Quaternary ammonium (R_4N^+) groups are key for NO_3^- removal, but their efficiency varies with water quality. This study developed a mixed-grafted ion exchange resin, CMIET-A, by grafting trimethylamine and triethylamine onto a poly(methyl methacrylate) backbone, with Ferromagnetic γ-Fe_2O_3 nanoparticles to enhance separability and recyclability. Experiments and DFT calculations showed that CMIET-A effectively removed NO_3^- across a broad pH range (4.0–10.0), with a maximum adsorption capacity of 82.79 mg/g. The adsorption behavior fit the Freundlich isotherm model, and the process followed the pseudo-second-order kinetic model. After 20 cycles, the resin maintained a NO_3^- removal rate over 70 %. Both experiments on the influence of external ions and Molecular dynamics simulations indicated higher binding energy and diffusion coefficients for CMIET-A with NO_3^-, enhancing performance even in the presence of Cl^-. Characterization revealed that ion exchange, pore filling, electrostatic attraction, hydrogen bonding, and metal bridging collectively drove adsorption. Overall, this novel resin offers an efficient solution for NO_3^- removal in industrial settings.

1. Introduction

Nitrate, as a quintessential persistent environmental pollutant, is characterized by its recalcitrance to degradation, high mobility [1], and strong stability, thereby persisting in the natural environment and posing a continuous threat to ecosystems [2]. The rapid development of industrial and agricultural activities has led to the improper discharge of substantial amounts of NO_3^--containing wastewater, resulting in a steady increase in NO_3^- concentrations in water bodies [3,4]. This phenomenon has far-reaching negative impacts on the safety of drinking water and the survival environment of aquatic organisms [5]. For instance, high concentrations of NO_3^- are a key driver of eutrophication in water bodies, which can trigger massive algal blooms, thereby disrupting the balance of aquatic ecosystems and affecting the survival and reproduction of aquatic organisms [4,6,7]. In view of the significant potential risks that NO_3^- poses to human health and the ecological environment, the World Health Organization (WHO) has explicitly stipulated that the concentration of NO_3^--nitrogen in drinking water should not exceed 10 mg/L [8].

Currently, various methods have been employed to remove excess NO_3^- from wastewater, including chemical co-precipitation [9], reduction [10], electrodialysis [11,12], microbial processes [13,14], and adsorption [15,16]. Among these, adsorption has gained widespread acceptance due to its simplicity [17], low energy consumption [18], and cost-effectiveness [19]. Common adsorbents encompass biochar [20], gels [21], metals [16], and metal oxides [22]. For instance, Tang et al. [15] enhanced the adsorption capacity of apple branch biochar through mechanical ball milling (MAB), KOH pre-treatment (K-MAB), and $MgCl_2/AlCl_3$ impregnation, achieving a maximum adsorption capacity of 43.70 mg/g for NO_3^-. Noha Amaly [23] fabricated a composite alginate aerogel by embedding montmorillonite particles containing cationic cetylpyridinium (MT^+) and further improved the NO_3^- adsorption capacity (795 mg/g) by grafting quaternary ammonium (QA) vinyl monomers to form MT^+@QAlg. Additionally, Pei et al. [24] and Qian et al. [25] achieved removal efficiencies of 82.56 % and 95 %, respectively, by loading nano-zero valent iron onto hydrotalcite and metal phenolic networks (MPNs). However, these adsorbents suffer from poor

* Corresponding author. State Key Laboratory of Coking Coal Resources Green Exploitation, China University of Mining and Technology, Xuzhou, 221008, China.
** Corresponding author.
E-mail addresses: 286717311@qq.com (W. Ke), babyxueyang@qq.com (Y. Xue), 8422127@alu.fudan.edu.cn (L. Feng), renxf@cumt.edu.cn (X. Ren).

https://doi.org/10.1016/j.pnsc.2026.01.003
Received 17 September 2025; Received in revised form 3 January 2026; Accepted 5 January 2026
Available online 18 February 2026

regeneration performance [26,27], intolerance to acids and alkalis [27], and inferior thermal stability [28], which collectively limit their application efficiency.

In modern water treatment industrial applications, ion exchange resins are widely used as important adsorbents. As a typical magnetic anion exchange resin, MIEX resin can effectively remove natural organic matter (NOM) [29–31], inorganic anions [32], and specific emerging contaminants [33], which has been successfully applied in drinking water treatment processes. Banu et al. [34] found that the adsorption of NO_3^- by the —$N(CH_3)_3$ functional group is spontaneous, thermodynamically favorable, endothermic, and entropy-driven. However, due to the diversity of pollutants, especially in the presence of chloride ions, MIEX resin does not perform well in NO_3^- removal [35]. Therefore, the direct use of MIEX resin to adsorb NO_3^- may not be a feasible technical method. Zhou et al. [36] increased the alkyl chain length of the quaternary ammonium salt sites on the resin (from methyl to ethyl) and found that this modification enhanced the hydrophobicity of the resin and improved its NO_3^- adsorption selectivity by reducing the hydration energy. However, the introduction of ethyl groups may reduce the total number of adsorption sites on the resin framework due to steric hindrance effects [37,38]. Therefore, it is feasible to design the preparation and functionalization of resins from the perspective of monomer synthesis to generate functional sites for preferential NO_3^- adsorption and to optimize the types and ratios of these sites to achieve the best microchemical structure of the adsorption sites, thereby realizing the efficient removal of NO_3^-. However, to date, no studies have reported the preparation of magnetic resins containing two types of adsorption sites for NO_3^- removal from water. The preparation methods, adsorption efficiencies, and mechanisms of such magnetic resins with these two types of adsorption sites are still unclear and require further investigation.

In this study, trimethylamine ($N(CH_3)_3$) and triethylamine ($N(C_2H_5)_3$) were employed as functional monomers to graft onto methacrylic resin (CMIET), resulting in the fabrication of three types of ion exchange resins, namely CMIET-A (grafted with trimethylamine), CMIET-M (grafted with triethylamine), and CMIET-E (grafted with a mixture of trimethylamine and triethylamine). Additionally, ferromagnetic γ-Fe_2O_3 nanoparticles were embedded into the resin as the core to enable efficient recovery without the need for an external magnetic field [36]. This improvement significantly shortens the process cycle and enhances treatment efficiency. The rapid magnetic separation technology reduces the need for large-scale structures such as sedimentation tanks, facilitating compact process design, which is particularly suitable for water treatment systems with limited space or modular configurations [39]. The physicochemical properties of the resins were characterized using scanning electron microscopy-energy dispersive spectroscopy (SEM-EDS), X-ray diffraction (XRD), Fourier-transform infrared spectroscopy (FTIR), and vibrating sample magnetometry (VSM), and their adsorption performance was evaluated through batch adsorption experiments. Subsequently, the adsorption isotherms, kinetics, and thermodynamics of the CMIET resins were systematically investigated, and the adsorption mechanisms and preferences for NO_3^- were elucidated using X-ray photoelectron spectroscopy (XPS) and density functional theory (DFT) calculations. Finally, the stability and reusability of the CMIET resins were assessed to evaluate their potential for practical applications.

2. Materials and methods

2.1. Chemicals

Ammonia ($NH_3{\cdot}H_2O$), Anhydrous Sodium Carbonate (Na_2CO_3), Ferrous Sulfate Heptahydrate ($FeSO_4{\cdot}7H_2O$), Hydrochloric Acid (HCl), Glycidyl Methacrylate (GMA), Anhydrous Ethyl Alcohol (C_2H_5OH), Oleic Acid ($C_{18}H_{34}O_2$), Potassium Bromide (KBr), Diethylbenzene (DVB), Cyclohexanol ($C_6H_{12}O$), Dodecyl Alcohol ($C12H_{26}O$), Polyvinyl Alcohol (PVA), Glycol polyoxyethylene ether (OP-10), Azo-Isobutyronitrile (AIBN), Polyester multichain polymer dispersants (HY-24000), Trimethylammonium Hydrochloride ($C_3H_{10}ClN$), Triethylamine Hydrochloride ($C_6H_{16}ClN$), Sodium chloride (NaCl), Potassium hydroxide (KOH). All reagents were analytical grade or better.

2.2. Preparation of materials

The schematic illustration of the resin synthesis in this study is shown in Fig. 1. The preparation of the resin primarily consists of three steps: the preparation and modification of γ-Fe_2O_3, the fabrication of the resin backbone, and the functionalization of the backbone. For more detailed descriptions of the first two steps, please refer to Section S2.

Grafting of functional groups: The preparation of the strong-base trimethylamine-type magnetic anion-exchange resin CMIET-M involved adding 4 g of the magnetic resin backbone CMIET to a 50 mL solution of NaCl (3.42 mol/L) and 1 % (w/w) NaOH. The mixture was stirred at 40 °C for 30 min to ensure complete dissolution and reaction. Subsequently, 10.4 g of trimethylamine was introduced into a solvent mixture comprising 1 mL of ammonia, 10 mL of deionized water, and 20 mL of anhydrous ethanol. This solution was then added to the CMIET backbone solution and allowed to react for 2 h at room temperature to obtain CMIET-M. The final product was washed with deionized water until neutral.

In a similar manner, the strong-base triethylamine-type magnetic anion-exchange resin CMIET-E was synthesized by dissolving 17.2 g of triethylamine salt in a mixture of 14 mL of deionized water, 2 mL of ammonia, and 32 mL of ethanol. This solution was added to the CMIT solution and stirred to form CMIET-E.

For the synthesis of the strong-base quaternary ammonium-type magnetic anion-exchange resin CMIET-A with dual functional groups, 6 g of the magnetic resin backbone CMIET was placed in a flask, to which 40 mL of water, 10 g of sodium chloride, and 10 mL of 5 % sodium hydroxide solution were added. The mixture was stirred and heated in a water bath for 30 min. Trimethylamine solution (3.4 g trimethylamine salt dissolved in 4 g of water, 0.3 mL of ammonia, and 7 mL of ethanol) and triethylamine solution (13.6 g triethylamine salt dissolved in 10 g of water, 1 mL of ammonia, and 20 mL of ethanol) were prepared separately and added to the flask. The reaction was carried out in a water bath for 3 h. After the reaction was complete, the sample was removed, soaked and stirred in dilute brine for 10 h, and finally washed with water to obtain CMIET-A.

2.3. Characterization of materials

In this study, a comprehensive characterization of the magnetic selective acrylic anion exchange resin for NO_3^- removal was conducted utilizing a variety of analytical techniques. X-Ray Diffraction (XRD) was employed to determine the crystallographic structure and phase purity of the synthesized γ-Fe2O3 and the resulting magnetic resin, with patterns recorded over a 2θ range of 5–85° using Cu Kα radiation. The magnetic properties, including saturation magnetisation and remanence, were quantified using a Vibration Sample Magnetometer (VSM) at room temperature, assessing the magnetic responsiveness crucial for the resin's separation and recovery in water treatment. Fourier-Transform Infrared Spectroscopy (FT-IR) analyzed the functional groups and chemical modifications on the resin surface, with spectra recorded after drying samples at 105 °C and preparing them as KBr pellets, indicating successful amine group grafting. Scanning Electron Microscopy (SEM) examined the morphology and surface topology of the magnetic resin particles, with samples sputter-coated with gold to enhance imaging, revealing a porous structure and particle size distribution. Brunauer-Emmett-Teller (BET) Surface Area Analysis determined the specific surface area, pore volume, and pore size distribution of the magnetic resin, with nitrogen gas adsorption-desorption isotherms measured at 77 K. Zeta Potential Measurements assessed the surface charge characteristics of the magnetic resin in aqueous media

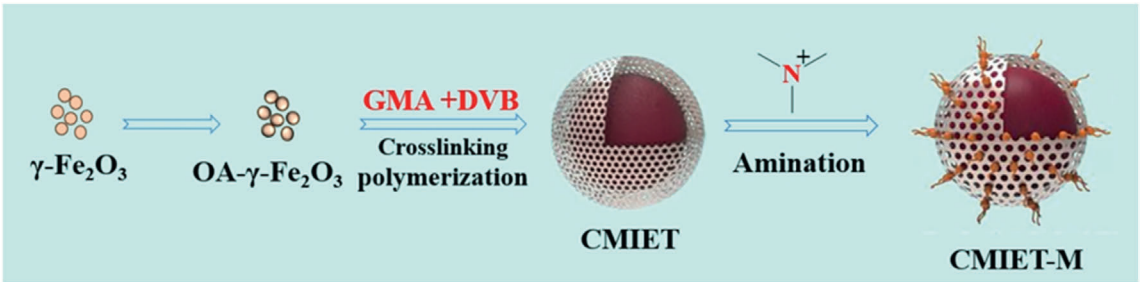

Fig. 1. Preparation process of magnetic CMIET series resins.

after thorough washing and dispersion in deionized water, providing insights into electrostatic interactions with NO_3^-. A Laser Particle Size Analyzer determined the size distribution and average particle diameter of the magnetic resin, offering data on particle uniformity and reactivity in suspension. Finally, X-Ray Photoelectron Spectroscopy (XPS) analyzed the chemical states and elemental composition of the resin surface before and after NO_3^- adsorption, confirming the proposed adsorption mechanisms through information on binding energies and chemical environments of the elements present.

2.4. Experimental and analysis methods

In this study, the adsorption performance of the resin was investigated using batch adsorption experiments with the control variable method. Specifically, the resin was mixed with the NO_3^- solution (500 mL, 100 mg/L) at a constant stirring speed of 400 rpm. The influence of resin dosage was examined by varying the amount of resin added. The effect of pH on the adsorption process was studied by adjusting the pH of the solution using 1 M HCl or NaOH. The adsorption equilibrium and kinetics of the resin were explored by varying the initial concentration of NO_3^- and the adsorption time. Finally, the adsorption thermodynamics of the resin were investigated by varying the initial temperature of the NO_3^- solution. Subsequently, samples were collected and filtered through a 0.45-μm syringe filter to obtain the supernatant. The residual NO_3^- concentration was then analyzed using a UV–Vis spectrophotometer at a wavelength of 220 nm. The adsorption capacity at equilibrium (Qe) was calculated using the formula

$$Q_e = \frac{(C_0 - C_e) \times V}{m}$$

where C_0 and C_e are the initial and equilibrium concentrations of NO_3^-, V is the volume of the solution, and m*m* is the mass of the adsorbent.

The percentage removal efficiency (η) was determined using the formula $\eta = \left(1 - \frac{C_e}{C_0} \times 100\%\right)$. Each experiment was performed in triplicate to ensure the reliability and reproducibility of the results. The data obtained were analyzed using origin software to model the experimental results against appropriate adsorption isotherms and kinetic models, thereby extracting relevant parameters and elucidating the mechanisms underlying NO_3^- adsorption onto the magnetic resins. In addition, the fitting equations are presented in Table S1.

2.5. Theoretical simulation

In this study, the two quaternary ammonium functional groups and the adsorption system of NO_3^- with the CMIET series resins was constructed using Materials Studio 2020 software. The geometric optimization of trimethylamine and triethylamine was performed using DMol3 with the GGA/PBE functional and Grimme's dispersion correction (DFT-D method). The calculations were carried out with unrestricted spin and a specified basis set. The resin structure was simplified to a poly(styrene-co-glycidyl methacrylate) chain containing 50 quaternary ammonium groups. The simplified resin, 6 NO_3^- ions, 6 Cl^- ions, and 500 water molecules were placed into a simulation cell using the amorphous cell module and the build layers function, and The initial periodic simulation box measures approximately 30 × 30 × 86 Å. In the forcite module, the COMPASS II force field was employed to simulate the polymer system, generating a stable molecular structure and performing ultra-fine geometry optimization. A dynamic equilibrium simulation of 10,000 steps was carried out under NPT integration conditions (pressure P = 0.0001 GPa, temperature T = 298 K, Timestep = 1.00 fs) to obtain a stable system density. Subsequently, the interaction energy (△E, in kJ/mol) was calculated based on the equation, and the diffusion behavior of NO_3^- in the adsorption system was evaluated using the mean square displacement (MSD).

$$\Delta E = E_{Total} - E_{NO_3^-} - E_{resin}$$

where E_{NO3} (kJ/mol) represents the total energy of the NO_3^- molecular structure, E_{resin} (kJ/mol) denotes the total energy of the resin structure, and E_{Total} (kJ/mol) signifies the total energy of the adsorption system.

3. Results and discussion

3.1. Characterization of porous magnetic anion exchange resins

Scanning electron microscopy (SEM) images (Fig. 2) reveal that, in contrast to the smooth surface of the CMIET skeleton (Fig. S1), the resin surface is significantly uneven with an intricate pore structure. This complex surface morphology is attributed to the incorporation of a large number of hydrophilic quaternary ammonium groups, which lead to the formation of dense cavities and channels, thereby constructing a complex hierarchical structure. Furthermore, the elemental distribution maps Fig. 2(g)–(l) of CMIET reveal a uniform distribution of iron (Fe) and nitrogen (N) throughout the material, indicating a high degree of homogeneity and consistency in the synthesis process. BET surface area analysis (as detailed in Table S2 and Fig. S2) indicated that all three resins possess a mesoporous structure. It is noteworthy that the specific surface area, pore volume, and pore diameter of the CMIET-A resin are 20.331 m^2/g, 0.0927 cm^3/g, and 18.24 nm, respectively, which are intermediate between those of CMIET-E and CMIET-M. These differences in properties are attributed to the presence of distinct functional groups in the resins. Specifically, the CMIET-M resin features a short-chain methyl group ($-CH_3$) as its activation group, in contrast to the CMIET-E resins, which contain a more extended ethyl group ($-CH_2CH_3$). The shorter alkyl chain in CMIET-M is to contribute to its enhanced surface area and reduced pore size, thereby augmenting the resin's overall porosity and specific surface area. Furthermore, the results of BET analysis indicate that the mixed-grafted material CMIET-A has a larger specific surface area and average pore size, second only to the long-chain uniformly grafted trimethylamine-functionalized material CMIET-M. The more and longer triethylamine functional groups loaded on CMIET-A cause significant steric hindrance due to the dense arrangement of alkyl chains during the adsorption process, which inhibits the entry of multivalent ions. This, in turn, reduces the steric

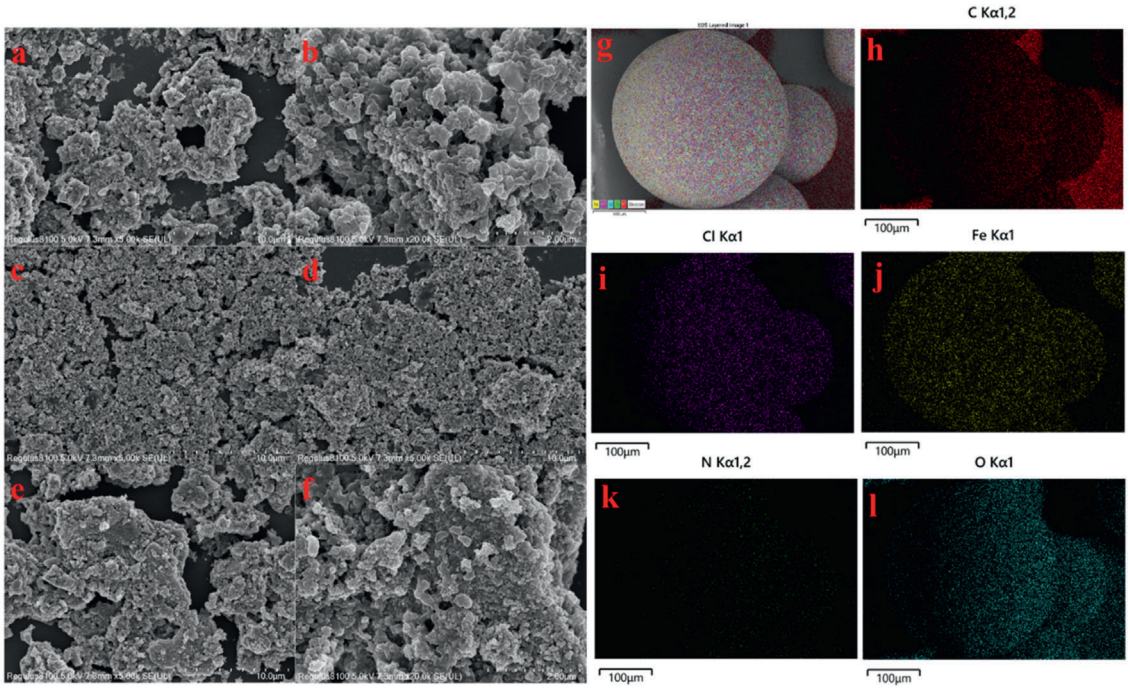

Fig. 2. SEM of porous magnetic resin: (a–b) CMIET-M, (c–d) CMIET-E, (e–f) CMIET-A; (g)–(l) EDS mapping scan image of CMIET-A.

hindrance for nitrate ions and increases the adsorption efficiency for nitrate ions.

The Fourier-transform infrared spectroscopy (FTIR) spectra of the magnetic resin skeletons CMIET, CMIET-M, CMIET-E, and CMIET-A were depicted in Fig. 3. A broad absorption band centered at 3447 cm^{-1} was observed and was assignable to the O-H stretching vibrations, indicative of the presence of hydroxyl groups within the resin matrix skeletons. This phenomenon may arise from the saponification reaction of some ester groups (O-C=O) in glycidyl methacrylate (GMA) induced by sodium hydroxide during the synthesis of quaternary ammonium functional groups. The weak bands at 2927 cm^{-1}, corresponding to the C-H stretching vibrations of methyl groups ($-CH_3$), and at 1731 cm^{-1}, attributed to the C=O stretching vibrations of ester (-C=O-) groups, confirmd the integrity of the basic structural components of the synthesized resins. A comparative analysis of the FTIR spectra reveals that no new absorption peaks were introduced in CMIET-M, CMIET-E, and CMIET-A relative to the pristine CMIET. However, a notable reduction in the intensity of the peaks associated with epoxy

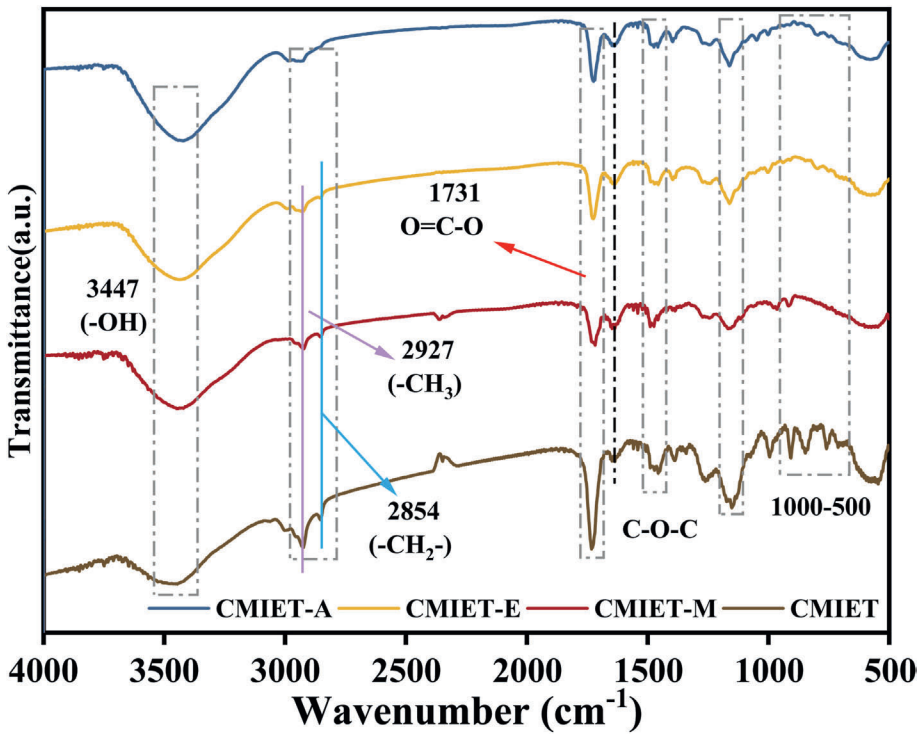

Fig. 3. FT-IR of magnetic anion resin CMIET.

groups (-O-CH_2-CH_3) was observed. This reduction suggested that the amine group (-NH2) had undergone a nucleophilic ring-opening reaction with the epoxy group (-O-CH_2-CH_3) on the resin skeleton, leading to the formation of a covalent bond. This observation provided compelling evidence for the successful activation and functionalization of the resin skeletons with the respective amine-containing moieties.

The resin was characterized by thermogravimetric analysis (TGA), as shown in Fig. 4(a)–(c), revealing that γ-Fe_2O_3 constitutes approximately 18.5 % of the magnetic material. The hysteresis curves (Fig. 4(d)–(f)) of CMIET-A, CMIET-M and CMIET-E showed that the hysteresis curves of the three resins do not exceed the zero point, and the saturation magnetisation strengths are 8.12 emu/g, 8.71 emu/g and 8.58 emu/g, respectively, and the residual magnetisation strengths are 2.06 emu/g, 2.213 emu/g and 2.19 emu/g, which showed that it is easy to enrich and separate, and because the ferromagnetic material used in this material is γ-Fe2O3, the resin particles themselves are self-aggregating, so they can be separated and recovered from the aqueous solution quickly under the environment of no magnetic field. Although the self-aggregation of the resin may reduce the accessible surface area and thus potentially negatively impact adsorption performance, this self-aggregation primarily occurs during the separation stage after adsorption is completed. During the adsorption process, moderate stirring (e.g., 400 rpm as used in the experiments) is sufficient to disrupt magnetic interactions, allowing the resin particles to disperse fully and ensuring effective contact with pollutants. Therefore, self-aggregation is a controlled, reversible behavior, and its negative impacts can be mitigated by adjusting operational conditions. Moreover, compared to the time-consuming gravitational sedimentation of traditional resins (which may lead to resin loss and extended operational cycles), the rapid and thorough separation induced by magnetism brings significant improvements in process efficiency, resin recovery rates, and operational reliability, which far outweigh the minor potential impacts on adsorption rates.

3.2. Analysis of the adsorption performance of magnetic resins

3.2.1. Effect of dosage

As illustrated in Fig. 5(a), the capacity for NO_3^- removal by the magnetic resins CMIET-M, CMIET-E, and CMIET-A is augmented with increasing dosage, a phenomenon attributed to the concomitant enlargement of the resins' total surface area and the concomitant proliferation of adsorptive sites, which in turn escalates the likelihood of interaction with NO_3^- [40]. The optimal dosage of 1.2 g/L was identified as a pivotal threshold for these resins, affording NO_3^- removal efficacies

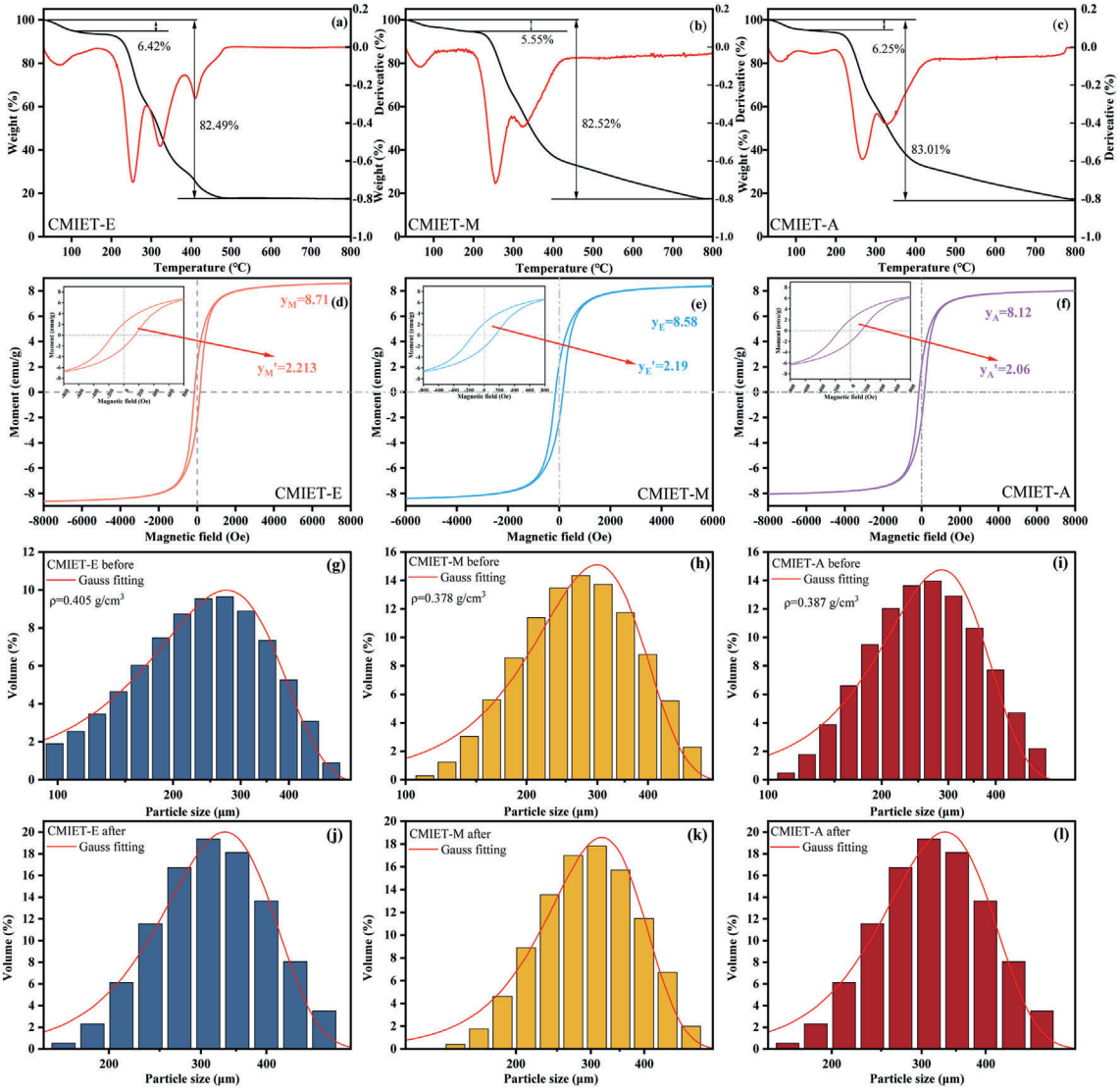

Fig. 4. Thermogravimetric curve of (a) CMIET-M, (b) CMIET-E, (c) CMIET-A; Hysteresis return curves of porous magnetic resin: (d) CMIET-M, (e) CMIET-E, (f) CMIET-A; Particle size distribution before and after resin adsorption (g)–(l).

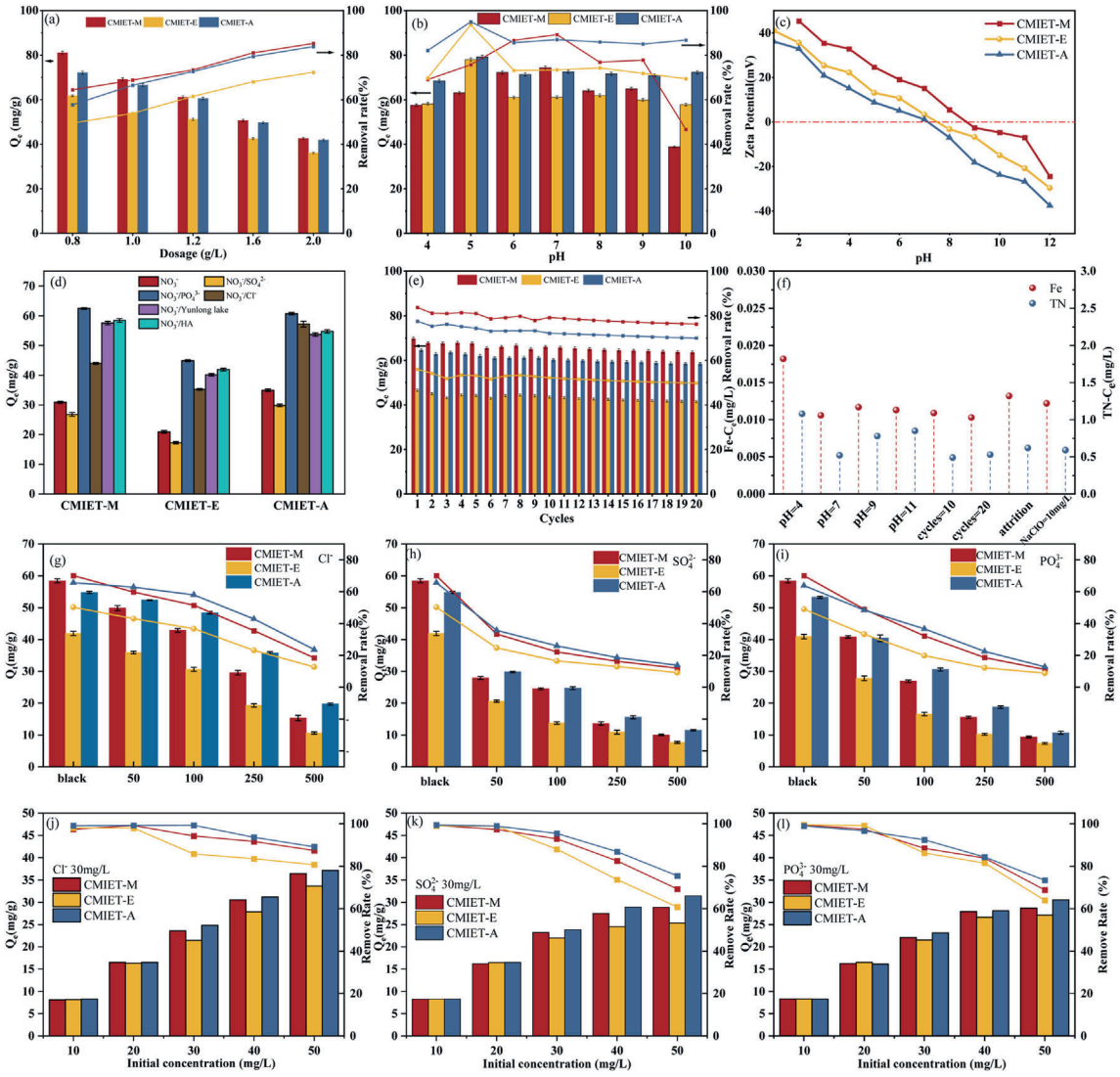

Fig. 5. The effects of dosage (a), pH (b), external ion and organic molecules (d), cycle number (e) on the adsorption of NO_3^- on CMIET resin; zeta point of CMIET resin (c); (f) Fe and N Leakage in Different Conditions; Effect of different extra ions concentrations on resin Adsorption of Nitrate with HA (10 mg/L) (g)–(i); Effects of Different extra ions at 10–50 mg/L NO_3^- on resin Adsorption (j)–(l). Background: Temperature: 293K, dosage: 1.2 g/L, time: 120 min, rotation speed: 150 rpm, initial concentration: 100 mg/L.

of approximately 73.4 %, 61.2 %, and 72.6 % for CMIET-M, CMIET-E, and CMIET-A, respectively. This dosage was selected for its efficacy in achieving a balance between cost-minimization and the attainment of adequate pollutant sequestration, thereby informing the protocol for subsequent experimental analyses. Additionally, similar experiments were conducted on the wet basis material, with the results shown in Fig. S3. It was found that the adsorption capacity of the wet basis material was comparable to that of the dry basis material. This may be attributed to the poly(methyl methacrylate) backbone we prepared, which has better hydrophilicity than the traditional polystyrene backbone, thereby maintaining a more open internal structure. Moreover, the embedded γ-Fe_2O_3 nanoparticles likely served as structural supports within the polymer network, preventing the complete collapse of pores in the dry state. These structural characteristics ensured that the quaternary ammonium functional groups within the resin were highly accessible in both dry and wet states.

3.2.2. *Effect of pH*

Fig. 5(b) elucidates the impact of pH on the adsorption of NO_3^- by resins. Observations indicate that the adsorption rates of NO_3^- by the three resins exhibit an increasing trend followed by a decrease as the pH value rises, reaching peak values at pH 5 or 6, with adsorption capacities of 73.24 mg/g, 78 mg/g, and 79.16 mg/g, respectively. Further analysis, as depicted in Fig. 5(c), shows that at pH = 7, the Zeta potentials of the three resins are 15.14 mV, 3.33 mV, and 1.13 mV, respectively, with their isoelectric points (IEP) all greater than 7. Consequently, at lower pH values, the resin surface becomes positively charged due to protonation, thereby facilitating adsorption of nitrate ions (NO_3^-) through the synergistic effects of electrostatic attraction and ion exchange. [2]. As the pH value increases from 4 to 5, the concentration of competitive chloride ions (Cl^-) introduced by the HCl used for pH adjustment gradually decreases, which in turn enhances the adsorption rate [41]. When the pH value ranges from 6 to 10, the concentration of OH- in water gradually increases, occupying active sites on the resin surface and competing with NO_3^- for adsorption sites [2,34]. Additionally, the Zeta potential measurements indicate that the resin surface gradually becomes negatively charged, transforming the electrostatic attraction between the resin and NO_3^- into electrostatic repulsion [42]. It is noteworthy that, although CMIET-M exhibits the most outstanding adsorption performance at pH 6 and 7, CMIET-A also shows excellent adsorption performance over a broader pH range and is less affected by pH changes. It is due to the quaternary ammonium is permanently

charged and not protonation-dependent. CMIET-E demonstrates a similar trend, with its adsorption performance being less influenced by pH. This phenomenon can be mainly attributed to the effect of the triethylamine functional groups. Compared with trimethylamine functional groups, triethylamine is less prone to excessive protonation under acidic conditions and less likely to undergo rapid deprotonation under alkaline conditions. Therefore, its adsorption performance is relatively less affected by pH changes and remains more stable.

Further corroborated by DFT calculations. The chemical interactions and active sites of the two quaternary ammonium functional groups were predicted through molecular electrostatic potential (MEP) analysis [43]. As shown in Fig. 6, the blue and red regions represent negative and positive electrostatic potentials, respectively. The nitrogen atoms in the quaternary ammonium groups (blue) exhibit the most negative electrostatic potential, while the positive charges are primarily localized on the hydrogen atoms, indicating their strong electrophilic nature. The nitrogen atoms in the triethylamine functional groups have higher electronegativity than those in the trimethylamine functional groups, implying that the hydrogen atoms in triethylamine have a stronger electrostatic attraction to nitrate ions (NO_3^-). Additionally, the chemical reactivity of different molecules was assessed using frontier molecular orbital (FMO) theory. The lowest unoccupied molecular orbital (LUMO) and the highest occupied molecular orbital (HOMO) typically represent the electron-accepting and electron-donating characteristics of a molecule, respectively [44]. As clearly seen in Fig. 6, the LUMO is predominantly localized on the C–H bonds, indicating that the alkyl groups play a crucial role in providing electrons to NO_3^-. Moreover, Fig. 6 show that trimethylamine has a lower LUMO energy (1.71 eV) than triethylamine

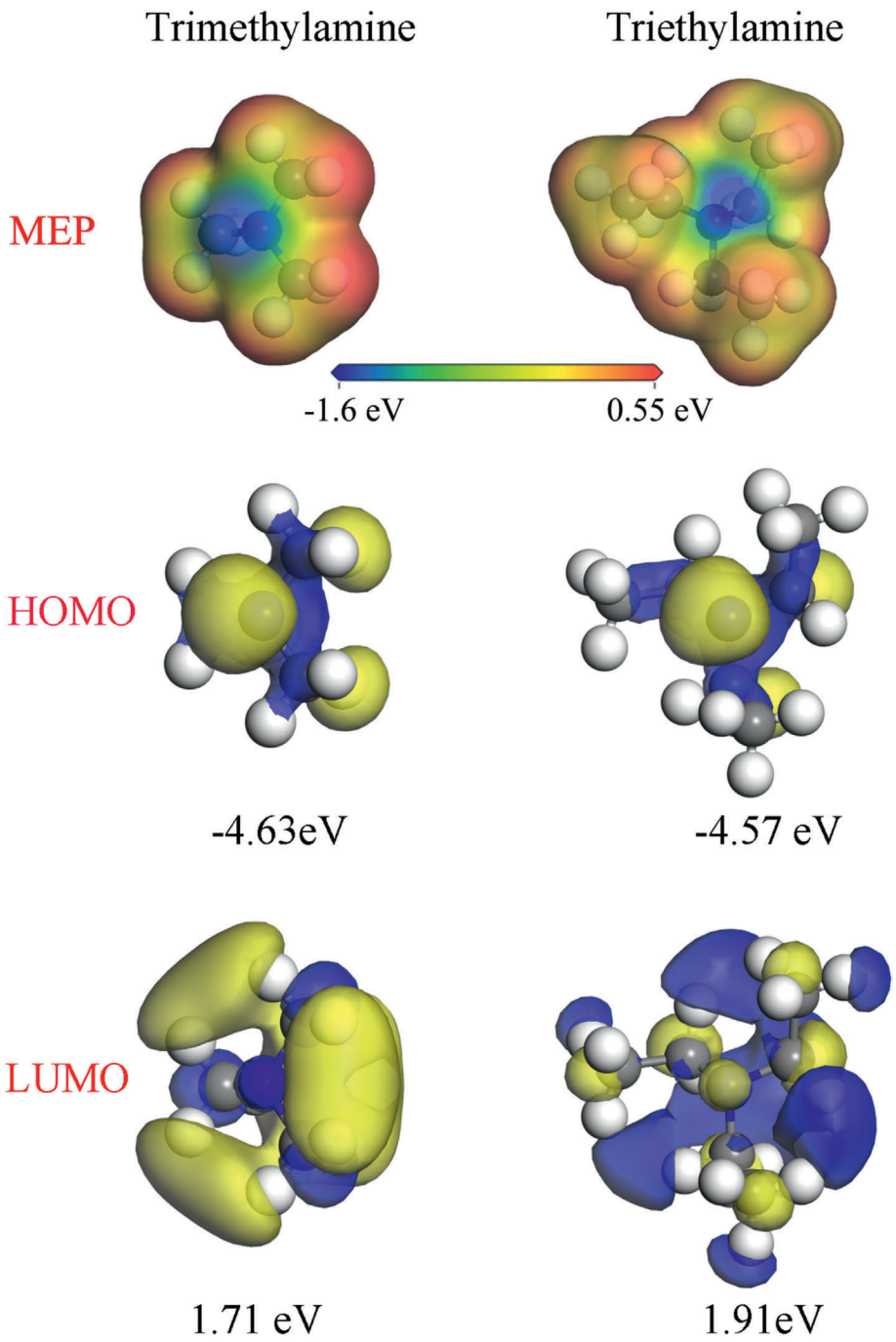

Fig. 6. Maps of molecular electrostatic potential (MEP), HOMO and LUMO for Trimethylamine and Triethylamine.

(1.91 eV), suggesting that trimethylamine is more prone to accepting electrons from protons, thereby facilitating protonation. This is one of the reasons why trimethylamine resin is more susceptible to pH variations in adsorption performance compared to triethylamine resin.

Since CMIET-A is a mixed-grafted resin, this structure enables it to have a more balanced adsorption performance under different pH conditions. Under acidic conditions, the trimethylamine part can contribute to the adsorption process, while the triethylamine part can also participate in the adsorption, providing additional adsorption sites or engaging in synergistic interactions with the adsorbate. Under alkaline conditions, the stable adsorption capacity of triethylamine can compensate for the reduced adsorption ability of trimethylamine. The experimental results show that, although the adsorption capacity of CMIET-A resin varies under different pH conditions, its overall adsorption ability remains strong, indicating that the resin has excellent acid and alkali resistance and is a highly promising material. Moreover, considering that the pH value of NO_3^--containing wastewater in actual industrial water bodies typically fluctuates around neutrality (6–9), the solution pH was adjusted to 7 in the subsequent experiments to better simulate real-world conditions.

3.2.3. Effect of external ions and organic molecules

Fig. 5(d) illustrates the impact of co-existing anions and organic molecules on the NO_3^- adsorption capacity of three types of resins, resulting in a varying degree of reduction. This phenomenon can be attributed to the competitive adsorption sites offered by the anions and organic molecules on the resin surface [45]. For the external ions, the influence of co-existing anions on the adsorption of NO_3^- by magnetic resins is as follows: $PO_4^{3-} > SO_4^{2-} > Cl^-$. The lower valence anion (Cl^-) exerts a minimal effect on the adsorption process, indicating that the magnetic resin CMIET-A exhibits a high selectivity for NO_3^- in the presence of high concentrations of Cl^-. In contrast, higher valence anions have a significant inhibitory effect on NO_3^- adsorption, which is not only due to competition for active adsorption sites but also due to steric hindrance effects from surface pores and functional groups, further exacerbating the adsorption barrier of NO_3^- [46]. Additionally, under the same molar concentration, higher valence anions carry more electrons, and due to the repulsion of like charges, the removal efficiency of NO_3^- tends to decrease [47]. The removal efficiency of NO_3^- is also related to the charge-to-radius ratio (z/r). Hu et al. [48] found that the charge-to-radius ratio of anions directly correlates with their affinity for adsorbents. The higher the charge-to-radius ratio, the stronger the affinity of the adsorbent, leading to stronger interactions [33]. The order of PO_4^{3-} (3/2.30) > SO_4^{2-} (2/2.24) > NO_3^- (1/1.65) > Cl^- (1/1.81) is consistent with their impact on NO_3^- removal efficiency. Similarly, to simulate real water bodies, this study investigated the effect of different concentrations of competing ions on nitrate adsorption in the presence of 10 mg/L of humic acid (HA, equivalent to approximately 5 mg/L dissolved organic carbon, DOC). As shown in Fig. 5(g)–(i), the influence of anions on the resin's adsorption of NO_3^- exhibited a similar trend to that in Fig. 5(d), with nitrate adsorption decreasing as the concentration of competing ions increased. Additionally, as shown in Table 1, the distribution coefficient Kd (L/g) for nitrate was highest for CMIET-A resin, consistent with the results in Fig. 5(d)–o. To further demonstrate the effect of different competing ions (30 mg/L) on nitrate adsorption at low concentrations (<50 mg/L) in Fig. 5(j)–(l). The results indicate that as the concentration of NO_3^- increased, the growth in adsorption capacity slowed and the removal rate began to decline due to the limited number of adsorption sites and competition from other ions. Nevertheless, under nitrate concentrations of less than 50 mg/L, the CMIET resin achieved nitrate adsorption efficiencies of over 85 %, and in some cases, complete adsorption.

It is noteworthy that, compared to CMIET-A and CMIET-E resins, CMIET-A demonstrates both a high adsorption capacity and stronger selectivity for NO_3^-. This may be attributed to the fact that it contains two quaternary ammonium functional groups at the same time. Relative to CMIET-E, CMIET-A incorporates trimethylamine, which has a lower molecular weight than triethylamine, facilitating more efficient activation and occupation of a greater adsorption space on the resin skeleton [49]. In contrast to CMIET-M, the introduction of long-chain ethylene groups in the quaternary ammonium functional groups renders CMIET-A more hydrophobic and confers a stronger electrostatic attraction, thereby enhancing its selectivity for NO_3^- adsorption [42,50]. The synergistic effects of these two types of functional groups endow CMIET-A with a robust NO_3^- removal capability, even in the presence of chloride salts.

3.2.4. Reusability, stability and compared with other adsorbents

In practical applications, the regenerative efficacy of an adsorbent is a critical metric for assessing its practical utility. In this study, we have selected a mixed solution of 0.1 M NaOH and 5 M NaCl as the regenerant. The specific regeneration procedure is as follows: 0.3 g of resin is placed in 500 mL of the regenerant solution and agitated at 150 rpm for 120 min at room temperature. After agitation, the resin is rinsed with deionized water until neutral and then reused for the next adsorption cycle. Additionally, the spent regenerant is collected in a dedicated alkali-resistant container for centralized treatment. As depicted in Fig. 5 (e), the capacity retention of the resins still keep in 90.22 %, 87.80 %, and 87.97 % of the initial removal efficiency, respectively, after 20 recycles. This decrement may be ascribed to the deactivation of some functional groups on the resin and the partial blockage of pores due to residual adsorbate [51]. Despite a slight decrease in adsorption efficiency, the CMIET series resins still exhibit excellent adsorption performance for NO_3^-, which can be primarily attributed to the stability of the CMIET backbone. As a result, CMIET-A demonstrates remarkable stability and reusability in the removal of NO_3^-. Additionally, we have made a rough estimation of the energy consumption and chemical costs per cubic meter of treated water. The cost associated with the core chemicals (mainly NaCl, with NaOH being secondary) is approximately 1.71 RMB, while the electricity cost for the entire process is only about 0.13 RMB. Thus, the total direct operating cost per cubic meter of treated water is estimated to be around 1.84 RMB.

Moreover, Fig. 7 illustrates that the CMIET resin particles aggregate into flocs in water due to their inherent magnetism, thereby significantly enhancing the sedimentation rate. As further demonstrated in Fig. 7 and Video 1, the CMIET resin achieves complete sedimentation within 20 s, with a sedimentation rate of 1.08 cm/s, facilitating rapid separation of the resin from water. This characteristic not only enables the use of lower resin concentrations and shorter retention times but also facilitates the implementation of continuous resin exchange and regeneration processes. Additionally, this addresses the issue of equipment footprint, reducing the spatial requirements.

Supplementary data related to this article can be found online at htt ps://doi.org/10.1016/j.pnsc.2026.01.003

Table 1
Nitrate distribution coefficients Kd (L/g) in different concentration of coexisting anions.

Samples	PO_4^{3-} (mg/L)			SO_4^{2-} (mg/L)			Cl^- (mg/L)		
	100	250	500	100	250	500	100	250	500
CMIET-M	0.3970	0.1916	0.1052	0.3086	0.1626	0.1135	0.8838	0.4585	0.1880
CMIET-E	0.2067	0.1166	0.0805	0.1650	0.1248	0.0843	0.4850	0.2512	0.1216
CMIET-A	0.4829	0.2419	0.1226	0.3512	0.1909	0.1331	1.1543	0.6260	0.2577

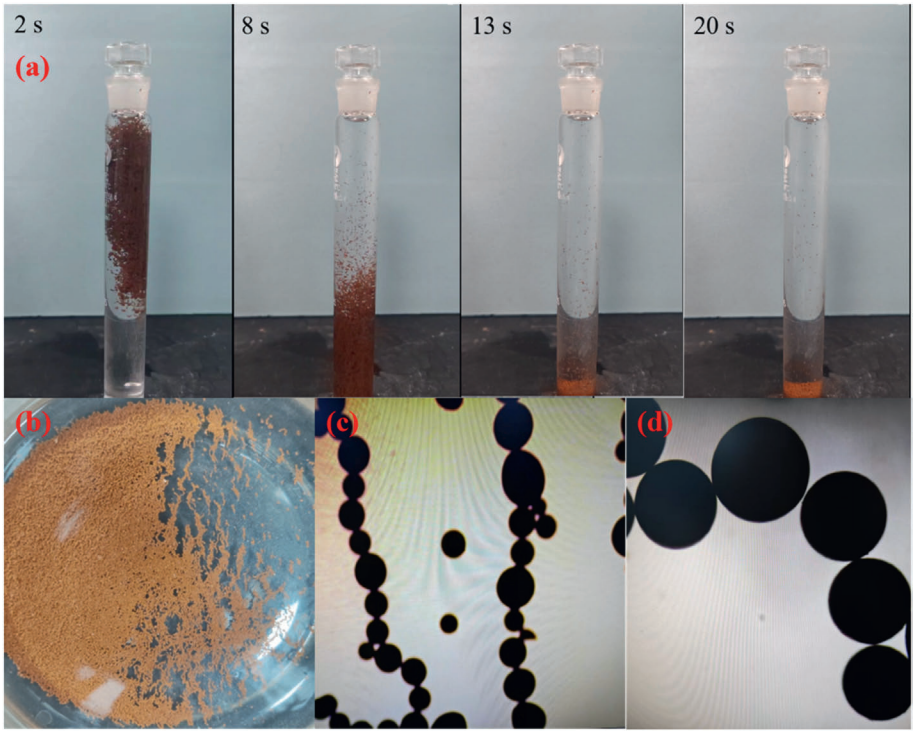

Fig. 7. (a)The settling diagram of CMIET resin in water; (b) The state of CMIET resin inwater; (c) magnetic field lines under a resin microscope.

To evaluate the stability of the resin, this study measured the content of iron (Fe) and nitrogen (N) in the resin under a pH range of 4–11, after 10 and 20 cycles of use, after abrasion, and after soaking in NaClO solution.as shown in Fig. 5(f), Through inductively coupled plasma (ICP) and total organic carbon (TOC) analysis, it was found that the resin exhibits extremely high stability. Even under acidic conditions with a pH of 4, the release of Fe and N was minimal, well below the World Health Organization (WHO) standard of 0.3 mg/L for Fe and the Chinese National Standard for Drinking Water (GB5749-2022) limit of 3 mg/L for total nitrogen (TN). This excellent stability is likely due to the resin's high chemical stability and low dosage. Additionally, the size variation of the resin after 20 adsorption cycles was investigated. The results showed that the resin size remained stable between 250 and 350 μm, with a slight increase in average size compared to the initial dimensions. This may be due to the incomplete desorption of ions and organic matter adsorbed on the resin over long-term use, which also explains the decreased efficiency in nitrate adsorption during cyclic use.

Furthermore, Table 2 summarizes previous studies on the removal of nitrate by different resins. Compared with other adsorbents, the porous magnetic resin synthesized in this study exhibits a higher adsorption capacity even at a temperature 5 °C lower than that typically used for conventional resins. Although two types of resins were reported to have higher adsorption performance than the CMIET resin, these resins lack ferromagnetism and thus do not match the separation efficiency of the CMIET resin. Overall, the CMIET resin not only has high adsorption capacity but also offers the advantage of easy separation and recycling, which strongly supports its further development and application.

Table 2
Comparison of synthesized porous magnetic resins with reported high adsorption performance resins for nitrate removal.

Samples	Temperature(K)	Q_e(mg/g)	References
PEGDA-MTAC	293	59.83	[52]
ALR-AE	298	44.41	[53]
CS-MNB	298	6.48	[54]
Relite A490	298	37.91	[55]
PHA-300W	298	3.6	[56]
D890	298	43.81	[57]
Purolite A 520E	298	142.6	[58]
L20	298	145.08	[59]
Skeleton CMIET	293	11.24	This study
CMIET-M	293	84.84	This study
CMIET-E	293	52.86	This study
CMIET-A	293	74.11	This study

3.3. Adsorption isotherm

The adsorption equilibrium experiments, as presented in Fig. 8(a)–(c), demonstrate that the adsorption capacity of NO_3^- on the resin increases with the enhancement of equilibrium concentration. This increment is attributed to the reduction in mass transfer resistance between the solid and liquid phases as a consequence of increased concentration [28]. Moreover, the adsorption capacity escalates with the elevation of temperature, a phenomenon attributed to the intensified motion of NO_3^- at higher temperatures, which augments the probability of interaction with the resin and consequently boosts the adsorption capacity [60]. Additionally, the increase in temperature reduces the viscosity of the solution, thereby facilitating the diffusion rate of NO_3^- through the external boundary layer into the internal structure of the resin, culminating in an increased adsorption capacity [61].

To delve deeper into the adsorption process of NO_3^- on the resin, the adsorption equilibrium data were fitted using both the Langmuir and Freundlich isotherm models. The fitting results, as depicted in Fig. 8(a)–(c) and Table 3, reveal that the Freundlich model exhibits higher correlation coefficients than the Langmuir model for all three types of resins. This suggests that the adsorption of NO_3^- on the resin is a heterogeneous multilayer process, characterized by non-uniform adsorption sites and the presence of multilayer stacking of NO_3^- on the resin [62]. This behavior is likely ascribed to the abundance of quaternary ammonium functional groups on the surface, which contribute to chemical adsorption, in conjunction with the dense porosity, which facilitates physical adsorption [63,64]. Furthermore, a value of n greater than 2 indicates that the adsorption process is facile [65,66].

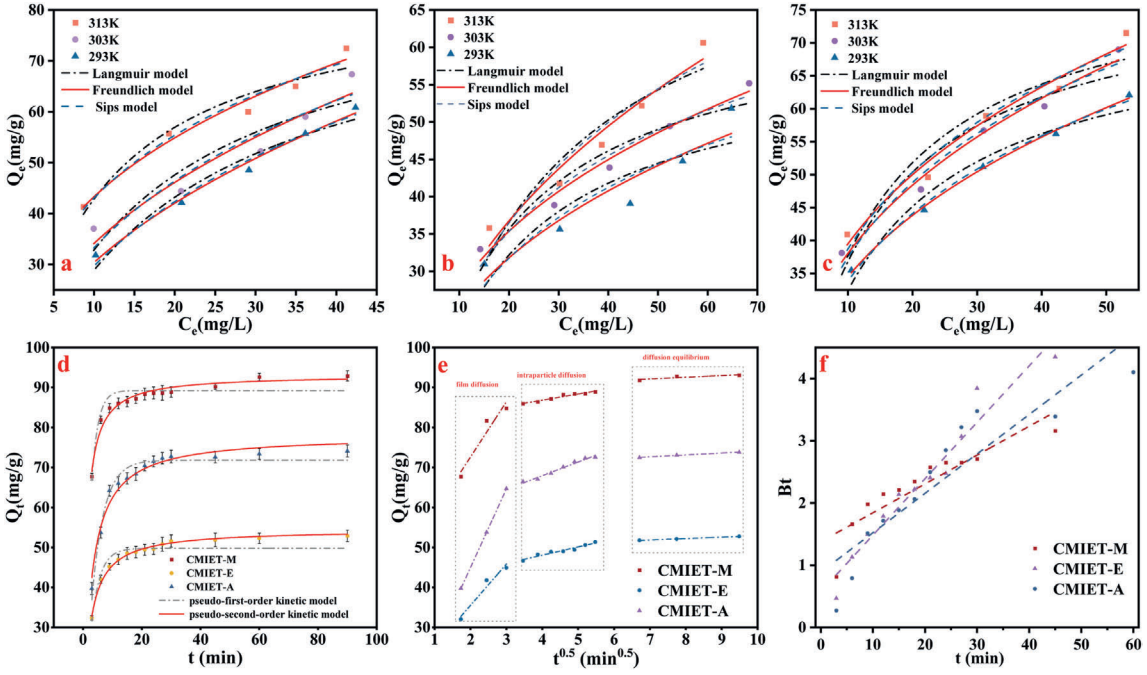

Fig. 8. The adsorption isotherms and fitting curves of NO_3^- on ion exchange resin at different temperatures: (a) CMIET-M,(b) CMIET-E, (c) CMIET-A; (d)Pesudo-first-order and second-order kinetic models; (e)Intra-particle diffusion model; (f) Boyd model for nitrate adsorption on CMIET resin.

Table 3
Isotherm constants for nitrate adsorption by magnetic resins at different temperatures.

Samples	Temp. (K)	Langmuir			Freundlich			Sips			
		Q_m(mg/g)	K_L	R^2	n	K_F	R^2	Q_m(mg/g)	ns	Ks	R^2
CMIET-M	293	84.84	0.102	0.92	2.92	19.70	0.96	161.17	0.66	0.010	0.98
	303	85.72	0.061	0.81	2.13	10.34	0.98	162.91	0.63	0.012	0.91
	313	86.38	0.050	0.84	2.30	12.56	0.90	166.27	0.51	0.013	0.97
CMIET-E	293	59.65	0.041	0.84	2.33	10.17	0.93	87.05	0.65	0.021	0.85
	303	65.29	0.060	0.87	2.88	12.53	0.97	93.89	0.64	0.023	0.95
	313	80.21	0.058	0.72	2.79	10.87	0.84	106.15	0.76	0.021	0.92
CMIET-A	293	74.39	0.083	0.88	2.93	18.03	0.96	148.73	0.52	0.009	0.99
	303	79.84	0.085	0.89	2.87	17.08	0.97	149.81	0.54	0.013	0.97
	313	82.79	0.077	0.95	2.88	15.53	0.99	152.70	0.53	0.013	0.96

Additionally, the Sips model was employed in this study to further analyze the adsorption process. The results indicated that the fitting curve was closer to the Freundlich model, with the parameter n_s consistently less than 1. This finding demonstrates the heterogeneity of the adsorbent surface, a broad distribution of adsorption site energies, and the presence of multiple adsorption sites with varying energy levels. Experimental findings reveal that the adsorption performance of CMIET-A for NO_3^- can reach a maximum of 50 mg/L at 293K, reflecting its superior adsorptive capacity (see Table 3).

3.4. Adsorption thermodynamics

In this study, the thermodynamic adsorption characteristics of NO_3^- on resins were investigated.

$$k_d = \frac{q_e}{C_e}$$

$$ln\ k_d = \frac{\Delta S}{R} - \frac{\Delta H}{RT}$$

$$\Delta G = \Delta H - T\Delta S$$

where the k_d is thermodynamic equilibrium constant, (L/g); ΔS is entropy change, (J/mol·K); ΔH is enthalpy change, (KJ/mol); ΔG is gibbs free energy, (KJ/mol); R is gas constant, 8.314 J/(mol·K) as see in Table 4. The values of ΔG° remain negative and decrease progressively with the increment of temperature, signifying that the adsorption process is a spontaneous endothermic reaction, with higher temperatures being conducive to adsorption. The range 40 kJ > ΔH > 0 suggests that the adsorption process involves both physical and chemical adsorption mechanisms [51,67]. A positive ΔS° indicates an increase in the complexity of the solid-liquid interface irregularity, with the randomness of the adsorption system escalating [68]. This randomness enhancement is attributed to the displacement of water molecules originally adsorbed on the adsorbent surface during the concurrent

Table 4
Thermodynamic parameters of CMIET-M, CMIET-E, CMIET-A.

Samples	Temp.(K)	ΔH^0 (kJ·mol^{-1})	ΔS^0 (J·mol^{-1}·K^{-1})	ΔG^0 (kJ·mol^{-1})
CMIET-M	293	7.765	29.52	−8.69
	303			−8.95
	313			−9.75
CMIET-E	293	7.561	27.04	−7.95
	303			−8.15
	313			−8.49
CMIET-A	293	5.725	20.73	−6.15
	303			−6.26
	313			−6.46

Table 5
Pesudo-first-order and second-order kinetic model constants for nitrate adsorption on porous magnetic resins at 293 K.

Samples	$Q_{e,exp}$ (mg/g)	Pesudo-first-order			Pesudo-second-order		
		$Q_{e,cal}$ (mg/g)	$10k_1$	R^2	$Q_{e,cal}$ (mg/g)	$100k_2$	R^2
CMIET-M	92.90	89.01	4.324	0.8718	91.97	1.201	0.9031
CMIET-E	52.86	51.39	2.760	0.8613	53.98	1.011	0.9915
CMIET-A	74.11	71.96	2.285	0.8557	75.22	0.5	0.9734

adsorption of NO_3^- [2], which is a favorable process for NO_3^- adsorption. Notably, compared to CMIET-M and CMIET-E, CMIET-A exhibits smaller absolute values for ΔH, ΔS, and ΔG°, yet it still demonstrates a high adsorption capacity for NO_3^-. This could be attributed to a higher proportion of physical adsorption in the adsorption process of CMIET-A.

3.5. Adsorption kinetic

Fig. 8(d) delineates the adsorption kinetics of NO_3^- onto three distinct resins. It is evident that the removal of NO_3^- is markedly rapid within the initial 30 min and reaches equilibrium within 45 min. The adsorption of NO_3^- onto the resins is predicated on the electrostatic attraction between NO_3^- and the grafted quaternary ammonium groups, thereby facilitating rapid adsorption [68]. Notably, CMIET-A exhibit superior adsorptive performance towards NO_3^-, which is attributed to the reduced steric hindrance conferred by the methylamine functional groups [69]. The adsorption kinetics fitting models and parameters (Table 5) indicate that the process predominantly conforms to the pseudo-second-order kinetic model ($R^2 = 0.9031$, 0.9915, 0.9734), suggesting that the adsorption is primarily a chemisorption process, involving the sharing or exchange of electrons between the resin and NO_3^- [70]. The particle diffusion model (Fig. 8(e)) reveal that the adsorption of NO_3^- onto the resins occurs in three distinct phases [71]: (1) Film diffusion: NO_3^- rapidly diffuse from the solution to the active adsorption sites on the resin surface, resulting in a swift increment in adsorption capacity; (2) Pore diffusion: As the adsorptive active sites on the resin surface gradually diminish, the adsorption rate decreases, and the adsorption capacity rises slowly as NO_3^- adsorbs from the resin surface into the internal pores and cavities; (3) Adsorption equilibrium: The adsorptive sites become saturated, and the repulsive forces between NO_3^- molecules in the liquid and solid phases reach a balance. Also, the analysis of the model parameters from Table 6(a) demonstrates that CMIET-A exhibits the highest adsorption capacity and rate, followed by CMIET-M and CMIET-E, respectively. This is evidenced by the highest $k_{ip,1}$, $k_{ip,2}$, and $k_{ip,3}$ values for CMIET-A, indicating its superior intraparticle diffusion rate. Furthermore, the intercept C values are all greater than zero, indicating that intraparticle diffusion is not the sole rate-determining stage in the adsorption process, which is also controlled by film diffusion [41]. Similarly, analysis using the Boyd model (Fig. 8(f) and Table 6(b)) indicates that the constant is not zero, suggesting that liquid film diffusion is a limiting factor in the adsorption process.

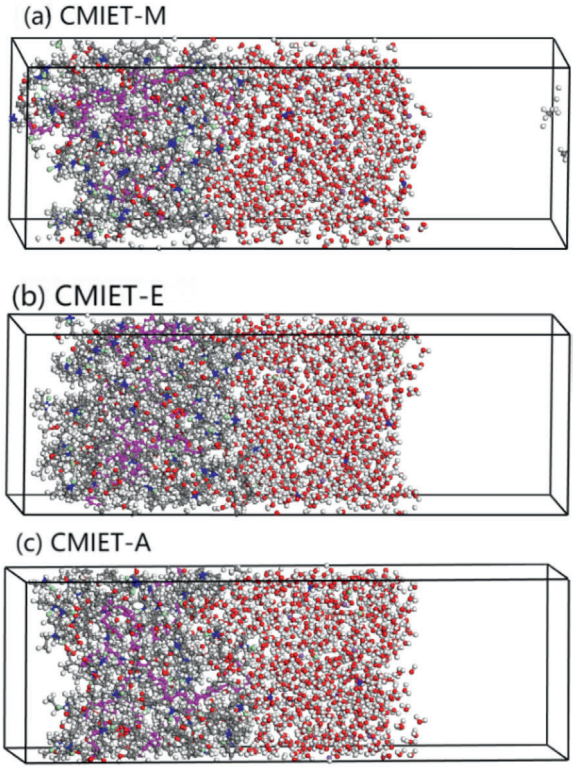

Fig. 9. The simulation adsorption systems and interaction energies of NO_3^- and CMIET resin.

3.6. Theoretical simulation

To explore the adsorption performance of CMIET-A for NO_3^- in the presence of NaCl, a simulated adsorption system of NO_3^- on CMIET resin was designed and constructed, and the interaction energy was calculated. As shown in Fig. 9 and Table, the interaction energies between NO_3^- and CMIET-A resin are all negative values, indicating that the adsorption processes are spontaneous, which is consistent with the conclusions in Section 3.1.3. Moreover, the order of the absolute values of interaction energies between NO_3^- and CMIET-A, CMIET-M, and CMIET-E is: CMIET-A > CMIET-M > CMIET-E, further confirming the excellent adsorption performance of CMIET-A for NO_3^-. Through molecular dynamics simulations, the diffusion coefficient of NO_3^- on CMIET resin was revealed from a theoretical calculation perspective. As shown in Table 6, the mean square displacement (MSD) value of CMIET-E is 0.2043 $Å^2$/ps, higher than that of CMIET-M (0.1751 $Å^2$/ps) and CMIET-

Table 6
Parameters of (a) intra-particle diffusion model and (b)Boyd model of nitrate adsorption by CMIET at 293K

(a) Samples	intra-particle diffusion modelling								
	$k_{ip,1}$ 95 % CI	C_1	R^2	$k_{ip,2}$ 95 % CI	C_2	R^2	$k_{ip,3}$ 95 % CI	C_3	R^2
CMIET-M	13.80 ± 3.86	45.02 ± 9.45	0.855	1.53 ± 0.17	80.71 ± 0.77	0.932	0.419 ± 0.21	89.21 ± 1.69	0.599
CMIET-E	10.32 ± 2.23	14.85 ± 5.46	0.910	2.06 ± 0.22	39.79 ± 1.02	0.933	0.354 ± 0.003	49.37 ± 0.031	0.999
CMIET-A	19.66 ± 0.06	5.65 ± 0.15	0.999	3.41 ± 0.24	54.28 ± 1.08	0.971	0.475 ± 0.05	69.33 ± 0.41	0.977

(b) Samples	Boyd model		
	K 95 % CI	B	R^2
CMIET-M	0.046 ± 0.008	1.379 ± 0.17	0.803
CMIET-E	0.09 ± 0.007	0.575 ± 0.16	0.946
CMIET-A	0.063 ± 0.009	0.888 ± 0.249	0.830

Table 7
The interaction energy calculation results and the value of mean square displacement (MSD).

	CMIET-M	CMIET-E	CMIET-A	CMIET-A-NO_3^-	CMIET-A-Cl^-	CMIET-A-SO_4^{2-}
ΔE(kcol/mol)	−203.016	−166.808	−226.177	−238.731	−205.272	−287.715
DMS(A^2/ps)	0.1751	0.1462	0.2043	0.2461	0.1893	0.2899

A (0.1462 $Å^2$/ps). This may be attributed to the fact that the structure of CMIET-A effectively reduces the spatial steric hindrance effect, enhances its interaction with NO_3^-, and thus reduces the resistance in the diffusion process. Furthermore, taking CMIET-A resin as an example, the influence of competing ions on nitrate adsorption was verified, as shown in Table 7. Among the competing ions, sulfate ions exhibit higher binding energy and diffusion coefficients than nitrate ions, whereas chloride ions have lower binding energy and diffusion coefficients than nitrate ions. This explains why sulfate ions have the greatest impact on adsorption, while chloride ions have the least impact in the competitive adsorption experiments. In summary, CMIET-A demonstrates outstanding adsorption performance for NO_3^- in the presence of NaCl. Its structural characteristics provide significant advantages in the adsorption process, offering theoretical support for practical adsorption applications.

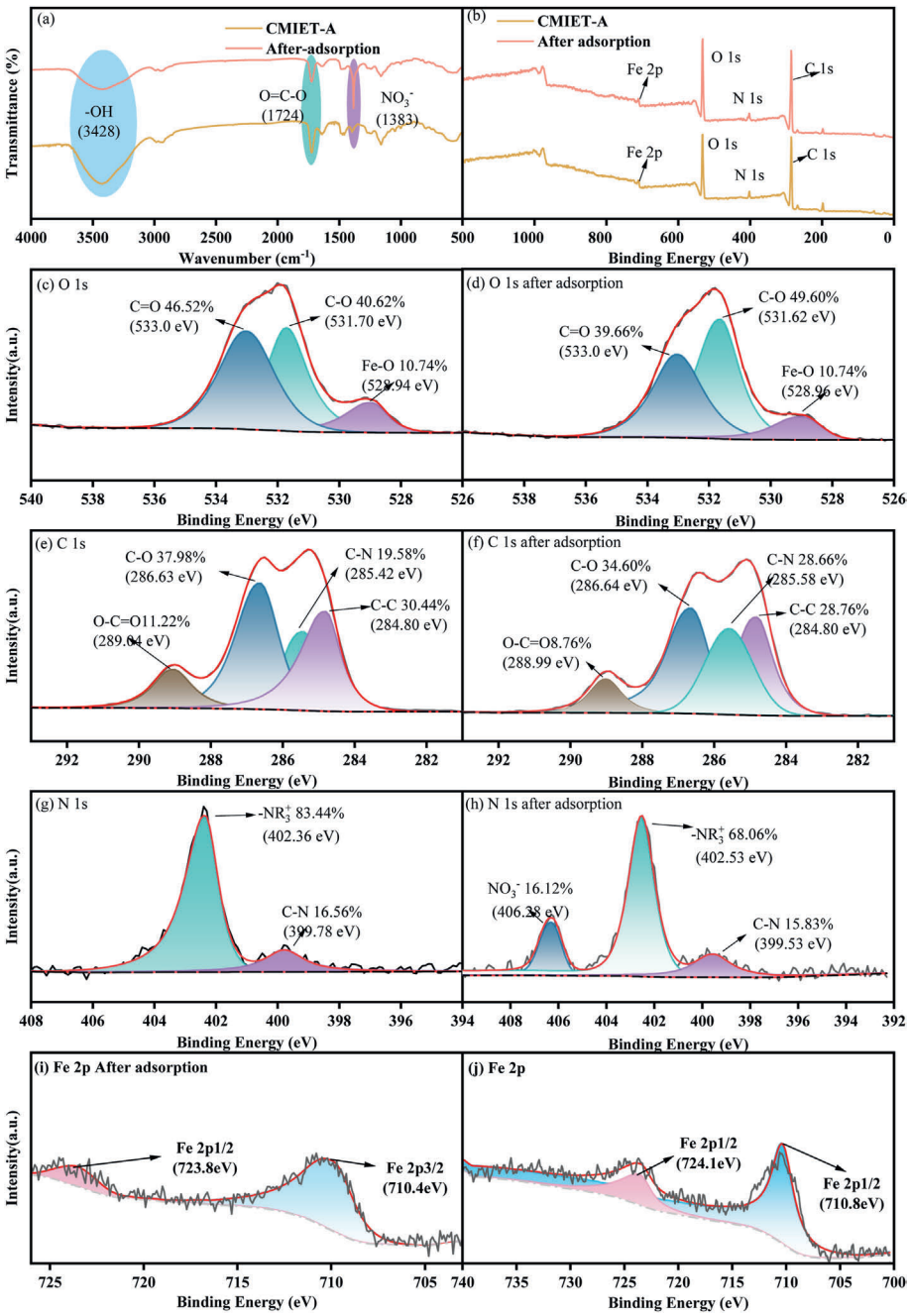

Fig. 10. Before and after nitrate adsorption: (a) FT-IR image; (b) full XPS image; (c),(d) O 1s XPS spectrum; (e),(f) C 1s XPS spectrum; (g),(h) N 1s XPS spectrum; (i), (j) Fe 2s XPS spectrum.

3.7. Mechanism of adsorption

Fourier-transform infrared (FT-IR, Fig. 10(a)) spectroscopy analysis before and after adsorption revealed that the stretching vibrations of NO_3^- led to a significant enhancement of the absorption peak at 1383 cm^{-1}, which further confirms the adsorption of NO_3^- on CMIET-M. Similarly, XPS wide-scan spectra (Fig. 10(b)) showed that, compared with pre-adsorption CMIET-A, the binding energy peaks of O and N on post-adsorption CMIET-A were significantly enhanced, which also proves the adsorption of NO_3^- on CMIET-A.

The adsorption thermodynamics and kinetics studies elucidated in the preceding text indicate that the adsorption of NO_3^- on CMIET-A is a composite process involving both physical and chemical adsorption, characterized by multilayer adsorption. The monolayer adsorption on the surface is predominantly chemical in nature, while the multilayer adsorption is primarily physical. Post-adsorption BET data (Table S2) reveal a reduction in the specific surface area, pore volume, and pore size of CMIET-E after adsorption, which substantiates the resin's NO_3^- adsorption via a pore-filling mechanism [72].

To further elucidate the chemical adsorption mechanism of NO_3^-, the XPS narrow spectra of CMIET-A were measured before and after adsorption. The O1s spectra (Fig. 9(c, d)) revealed that the relative area of the C=O peak decreased from 46.52 % to 39.66 %. Meanwhile, the C1s spectra (Fig. 10(e) and (f)) showed that the area of the O-C=O peak decreased from 11.22 % to 8.76 %, and the binding energy shifted from 289.04 eV to 288.99 eV. These changes indicate a significant alteration in the chemical environment surrounding the C=O group, thereby confirming the presence of hydrogen bonding interactions between C=O and NO_3^-. Additionally, Fig. 10(a) shows that the -OH peak (3428 cm^{-1}) and O=C-O peak (1724 cm^{-1}) were attenuated to a certain extent after adsorption, further demonstrating the hydrogen bonding interactions between the functional groups of the resin and NO_3^-. The post-adsorption C1s spectra (Fig. 10(e) and (f)) also revealed that the proportion of the C-N peak increased from 19.58 % to 28.66 %, and the binding energy shifted from 285.42 eV to 285.58 eV. This phenomenon can be attributed to the attraction between the electron clouds of the carbon atoms adsorbed on the quaternary ammonium functional groups and the nitrogen atoms in NO_3^-. The enhanced interaction between them increases the electron density around the carbon atoms, thereby enhancing the signal intensity of the C-N peak. The N 1s spectra (Fig. 10 (g) and (h)) more clearly show the enhancement of the N 1s characteristic peak after adsorption, further confirming the adsorption of NO_3^- by CMIET-A. The pre- and post-adsorption N 1s narrow-scan spectra show that the peak corresponding to protonated amine [7] (-N^+, 402.36 eV) shifted by 0.17 eV, and a typical NO_3^- peak (406.34 eV) appeared after adsorption. These results indicate that the quaternary ammonium groups on the resin surface adsorbed NO_3^- through electrostatic attraction and ion exchange. Furthermore, Fig. 10(i), (j) shows that a slight decrease in the Fe 2p peak area and a shift in the binding energies of Fe 2p1/2 and Fe 2p3/2 from 724.1 eV to 710.8 eV–723.8 eV and 710.4 eV, respectively, suggest that NO_3^- may be adsorbed onto the resin through metal bond bridging involving the iron core [73].

The adsorption mechanism is depicted in Fig. 11. In summary, the adsorption process involves NO_3^- contacting the material surface, diffusing through pores into the abundant internal channels, undergoing ion exchange with chloride ions, electrostatic interactions with quaternary ammonium groups on the resin surface, surface metal bond bridging with trivalent iron, and hydrogen bonding with oxygen-containing functional groups (-COOH, -OH). Collectively, these interactions accomplish the adsorptive removal of NO_3^-.

4. Conclusion

This study has successfully developed a novel mixed-grafted ion exchange resin, CMIET-A, for efficient NO_3^- removal from water. Comprehensive experimental results demonstrated that CMIET-A exhibited superior adsorption performance for NO_3^- over a wide pH range (4.0–11.0), achieving a maximum adsorption capacity of approximately 82.79 mg/g. The adsorption process was well described by the Freundlich isotherm model and the pseudo-second-order kinetic model. Characterization results indicated that the adsorption mechanism is a heterogeneous multilayer process, dominated by ion exchange and involving electrostatic attraction, hydrogen bonding, and metal bridging. The resin maintained a NO_3^- removal rate of over 70 % after 10 adsorption-desorption cycles, highlighting its stability and reusability. Molecular dynamics simulations further revealed that the higher binding energy and molecular diffusion coefficient between CMIET-A and NO_3^- contributed to its excellent adsorption performance, even in the

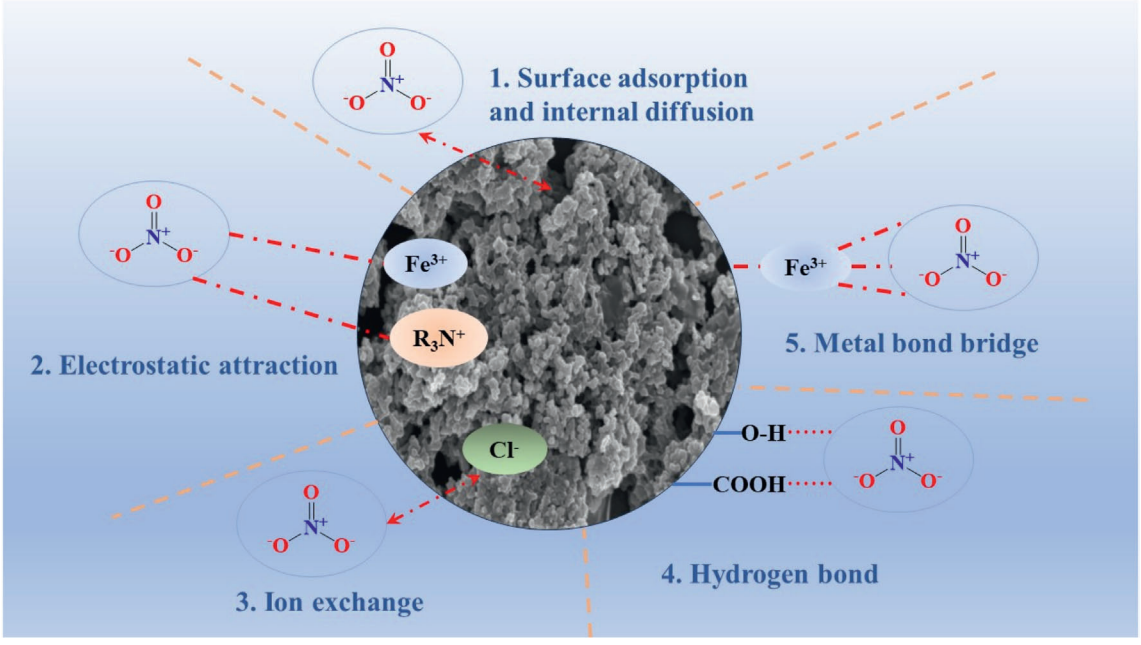

Fig. 11. Mechanism of nitrate removal by porous magnetic resin.

presence of competing chloride ions. Overall, this study introduces a promising adsorbent for NO_3^- removal, offering a potential solution to address NO_3^- pollution in industrial and environmental contexts. Future work should focus on scaling up the resin synthesis and conducting pilot-scale studies to evaluate its long-term performance and economic feasibility in real-world applications.

CRediT authorship contribution statement

Yiming Zong: Writing – review & editing, Writing – original draft, Software, Resources, Methodology, Investigation, Data curation, Conceptualization. **Wenjiao Ke:** Funding acquisition. **Yang Xue:** Funding acquisition. **Rui Xiao:** Resources, Conceptualization. **Sixi Zhu:** Visualization. **Shuya Zheng:** Software, Resources. **Yongen Shi:** Validation, Supervision. **Li Feng:** Supervision, Software, Resources, Funding acquisition. **Xuefeng Ren:** Supervision, Software, Resources, Methodology.

Declaration of competing interest

The authors declare the following financial interests/personal relationships which may be considered as potential competing interests:Li Feng reports financial support and equipment, drugs, or supplies were provided by Feng Li's group, School of Chemical Engineering, China University of Mining and Technology, China. Li Feng reports a relationship with Feng Li's group, School of Chemical Engineering, China University of Mining and Technology, China that includes: funding grants and non-financial support. If there are other authors, they declare that they have no known competing financial interests or personal relationships that could have appeared to influence the work reported in this paper.

Acknowledgement

The authors acknowledge the financial support from Jiangsu Provincial Key Research and Development Program (BE2021632); Power Construction Corporation of China (KJ-2023-100); China Power Construction Corporation Limited Science and Technology Projects (DJ-ZDXM-2023-23); China University of Mining and Technology (CUMT) Open Sharing Fund for Large-scale Instruments and Equipment. The authors extend their gratitude to Mr Luo Huan (from Scientific Compass www.shiyanjia.com) for providing invaluable assistance with the SEM analysis.

Appendix A. Supplementary data

Supplementary data to this article can be found online at https://doi.org/10.1016/j.pnsc.2026.01.003.

References

[1] Y. Hao, T. Zheng, L. Liu, P. Li, H. Ma, Z. Zheng, X. Zheng, J. Luo, Occurrence of dissimilatory nitrate reduction to ammonium (DNRA) in groundwater table fluctuation zones during dissolved organic nitrogen leaching through unsaturated zone, J. Hazard Mater. 489 (2025) 137501, https://doi.org/10.1016/j.jhazmat.2025.137501.

[2] Y. Shen, N. Chen, Z. Feng, C. Feng, Y. Deng, Treatment of nitrate containing wastewater by adsorption process using polypyrrole-modified plastic-carbon: characteristic and mechanism, Chemosphere 297 (2022) 134107, https://doi.org/10.1016/j.chemosphere.2022.134107.

[3] Y. Zhang, M. Ren, J. Su, Y. Bai, X. Li, Y. Wang, Simultaneous removal of carbamazepine, nitrate, and copper in a biofilm reactor filled with FeMn-modified ceramsite, J. Hazard Mater. 491 (2025) 137871, https://doi.org/10.1016/j.jhazmat.2025.137871.

[4] C. Hou, Y. Wang, J. Su, M. Ren, X. Wang, Y. Wang, Simultaneous removal of nitrate, copper, carbamazepine, and calcium from micropolluted water by fulvic acid through promotion of denitrification and microbial-induced calcium precipitation: performance and mechanism, Bioresour. Technol. 415 (2025) 131695, https://doi.org/10.1016/j.biortech.2024.131695.

[5] W. Hu, L. Wang, K. Zhu, F. Wu, H. Qiao, Y. Li, Facile copolymerization synthesis of vinylimidazole/dibromodecane/vinylpyridine polymer with high capacity for selective adsorption of nitrate from water, J. Water Proc. Eng. 49 (2022) 103052, https://doi.org/10.1016/j.jwpe.2022.103052.

[6] A. Marí, J.A. Baeza, L. Calvo, M.A. Gilarranz, Treatment of nitrate-polluted natural waters by reduction in catalytic membrane contact reactors, Separ. Purif. Technol. 358 (2025) 130261, https://doi.org/10.1016/j.seppur.2024.130261.

[7] S. Lu, Q. Zhu, R. Li, Selective adsorption of nitrate in water by organosilicon quaternary ammonium salt modified derived nickel-iron layered double hydroxide: adsorption characteristics and mechanism, J. Colloid Interface Sci. 652 (2023) 1481–1493, https://doi.org/10.1016/j.jcis.2023.08.150.

[8] J. Chen, J. Hu, K. Zuo, X. Li, L. Zhang, Unexpected electrosorption capacity and selectivity of fungal hyphae derived carbon film for nitrate removal, Separ. Purif. Technol. 362 (2025) 131676, https://doi.org/10.1016/j.seppur.2025.131676.

[9] T.K.M. Prashantha Kumar, T.R. Mandlimath, P. Sangeetha, S.K. Revathi, S.K. Ashok Kumar, Nanoscale materials as sorbents for nitrate and phosphate removal from water, Environ. Chem. Lett. 16 (2018) 389–400, https://doi.org/10.1007/s10311-017-0682-7.

[10] H.O. Tugaoen, P. Herckes, K. Hristovski, P. Westerhoff, Influence of ultraviolet wavelengths on kinetics and selectivity for N-gases during TiO2 photocatalytic reduction of nitrate, Appl. Catal. B Environ. 220 (2018) 597–606, https://doi.org/10.1016/j.apcatb.2017.08.078.

[11] M. Gu, Y. Wang, D. Wan, Y. Shi, Q. He, Electrodialysis ion-exchange membrane bioreactor (EDIMB) to remove nitrate from water: optimization of operating conditions and kinetics analysis, Sci. Total Environ. 839 (2022) 156046, https://doi.org/10.1016/j.scitotenv.2022.156046.

[12] M.C. Martí-Calatayud, M. Ruiz-García, V. Pérez-Herranz, On the selective transport of mixtures of organic and inorganic anions through anion-exchange membranes: a case study about the separation of nitrates and citric acid by electrodialysis, Separ. Purif. Technol. 354 (2025) 128951, https://doi.org/10.1016/j.seppur.2024.128951.

[13] Y. You, A sustainable approach for removing nitrate: studying the nitrate transformation and metabolic potential under different carbon source by microorganism, J. Clean. Prod. 346 (2022) 131169, https://doi.org/10.1016/j.jclepro.2022.131169.

[14] X. Zhou, C. Zhang, Y. Li, Time-delayed photocatalysis enhanced microbial nitrate reduction via solar energy storage in carbon nitrides, Chem. Eng. J. 417 (2021) 127904, https://doi.org/10.1016/j.cej.2020.127904.

[15] Y. Tang, X. Zhang, Q. Yang, Y. Yan, W. Ding, W. Du, F. Hu, Z. Geng, C. Xu, Enhanced removal of the ammonium, nitrate and phosphate by biochars derived from apple tree branches via different modification methods, Separ. Purif. Technol. 362 (2025) 131740, https://doi.org/10.1016/j.seppur.2025.131740.

[16] S. Fang, J. Zhang, Y. Niu, S. Ju, Y. Gu, K. Han, X. Wan, N. Li, Y. Zhou, Removal of nitrate nitrogen from wastewater by green synthetic hydrophilic activated carbon supported sulfide modified nanoscale zerovalent Iron: characterization, performance and mechanism, Chem. Eng. J. 461 (2023) 141990, https://doi.org/10.1016/j.cej.2023.141990.

[17] L.K. Njaramba, S. Kim, Y. Kim, B. Cha, N. Kim, Y. Yoon, C.M. Park, Remarkable adsorption for hazardous organic and inorganic contaminants by multifunctional amorphous core–shell structures of metal–organic framework-alginate composites, Chem. Eng. J. 431 (2022) 133415, https://doi.org/10.1016/j.cej.2021.133415.

[18] T. Wang, D. Zhang, K. Fang, W. Zhu, Q. Peng, Z. Xie, Enhanced nitrate removal by physical activation and mg/al layered double hydroxide modified biochar derived from wood waste: adsorption characteristics and mechanisms, J. Environ. Chem. Eng. 9 (2021) 105184, https://doi.org/10.1016/j.jece.2021.105184.

[19] H. Zhao, X. Huang, Y. Yang, L. Wang, X. Zhao, F. Yan, Y. Yang, P. Gao, P. Ji, The role of available nitrogen in the adsorption of polystyrene nanoplastics on magnetic materials, Water Res. 229 (2023) 119481, https://doi.org/10.1016/j.watres.2022.119481.

[20] K. Vijayaraghavan, R. Balasubramanian, Application of pinewood waste-derived biochar for the removal of nitrate and phosphate from single and binary solutions, Chemosphere 278 (2021) 130361, https://doi.org/10.1016/j.chemosphere.2021.130361.

[21] M. Velu, B. Balasubramanian, P. Velmurugan, H. Kamyab, A.V. Ravi, S. Chelliapan, C.T. Lee, J. Palaniyappan, Fabrication of nanocomposites mediated from aluminium nanoparticles/Moringa oleifera gum activated carbon for effective photocatalytic removal of nitrate and phosphate in aqueous solution, J. Clean. Prod. 281 (2021) 124553, https://doi.org/10.1016/j.jclepro.2020.124553.

[22] Y. Lu, H. Zhang, Y. Li, Coupling FeMgAl-LDH and sludge biofilm for simultaneous and effective removal of nitrate and ammonium in water, J. Water Proc. Eng. 56 (2023) 104285, https://doi.org/10.1016/j.jwpe.2023.104285.

[23] N. Amaly, C. Douglas, G. Sun, P.K. Pandey, Development of a high-performance alginate-based composite aerogel for adsorption and recovery of phosphate and nitrate from livestock wastewater, Separ. Purif. Technol. 362 (2025) 131820, https://doi.org/10.1016/j.seppur.2025.131820.

[24] Y. Pei, W. Cheng, R. Liu, H. Di, Y. Jiang, C. Zheng, Z. Jiang, Synergistic effect and mechanism of nZVI/LDH composites adsorption coupled reduction of nitrate in micro-polluted water, J. Hazard Mater. 464 (2024) 133023, https://doi.org/10.1016/j.jhazmat.2023.133023.

[25] Y. Qian, P. Wan, A.S. Hursthouse, G. Zhu, A novel zero-valent iron/titanium tannate composite for deep removal of nitrogen from water, Chem. Eng. J. 508 (2025) 160937, https://doi.org/10.1016/j.cej.2025.160937.

[26] Z. He, C. Wang, H. Cao, J. Liang, S. Pei, Z. Li, Nitrate absorption and desorption by biochar, Agronomy 13 (2023) 2440, https://doi.org/10.3390/agronomy13092440.

[27] E. Priya, S. Kumar, C. Verma, S. Sarkar, P.K. Maji, A comprehensive review on technological advances of adsorption for removing nitrate and phosphate from waste water, J. Water Proc. Eng. 49 (2022) 103159, https://doi.org/10.1016/j.jwpe.2022.103159.
[28] Y. Liu, X. Zhang, J. Wang, A critical review of various adsorbents for selective removal of nitrate from water: structure, performance and mechanism, Chemosphere 291 (2022) 132728, https://doi.org/10.1016/j.chemosphere.2021.132728.
[29] L. Yang, Z. Chen, Y. Tang, Q. Wen, Evaluation of magnetic ion-exchange resin for oxytetracycline removal in secondary effluent: behavior, mechanisms and theoretical calculation, Separ. Purif. Technol. 361 (2025) 131333, https://doi.org/10.1016/j.seppur.2024.131333.
[30] J. Zhang, W. Wu, Y. Gao, S. Zhao, Y. Zong, G. Xue, Y. Song, L. Ding, Efficient removal of nitrophenol by magnetic ion exchange resins: role of nitrophenol functional groups based on characterisation, DFT calculations and site energy distributions, Separ. Purif. Technol. 354 (2025) 129096, https://doi.org/10.1016/j.seppur.2024.129096.
[31] I. Palee, S. Kaewsimmaporn, P. Jutaporn, P. Phungsai, T. Ratpukdi, Reverse osmosis pretreatment by a fluidized magnetic ion exchange resin for application in a power plant: Pilot-scale and high-rate operations and foulant characterization, Chem. Eng. J. 470 (2023) 144320, https://doi.org/10.1016/j.cej.2023.144320.
[32] L. Ding, H. Deng, C. Wu, X. Han, Affecting factors, equilibrium, kinetics and thermodynamics of bromide removal from aqueous solutions by MIEX resin, Chem. Eng. J. 181–182 (2012) 360–370, https://doi.org/10.1016/j.cej.2011.11.096.
[33] Y. Tang, Q. Wen, Z. Chen, B. Yang, H.-Y. Hu, Different mobile counter ion types of magnetic ion-exchange resin coupling with ozonation treatment of the organic matter, antibiotic resistance genes, and pathogens in secondary effluent, Chem. Eng. J. 485 (2024) 149962, https://doi.org/10.1016/j.cej.2024.149962.
[34] H.T. Banu, S. Meenakshi, Synthesis of a novel quaternized form of melamine–formaldehyde resin for the removal of nitrate from water, J. Water Proc. Eng. 16 (2017) 81–89, https://doi.org/10.1016/j.jwpe.2016.12.003.
[35] C. Liu, L. Zhu, G. Zhang, J. Wang, Y. Deng, W. Chen, Removal of nitrate from ground water by miex resins, Fresenius Environ. Bull. 25 (2016) 316–324.
[36] Y. Zhou, C.D. Shuang, Q. Zhou, M.C. Zhang, P.H. Li, A.M. Li, Preparation and application of a novel magnetic anion exchange resin for selective nitrate removal, Chin. Chem. Lett. 23 (2012) 813–816, https://doi.org/10.1016/j.cclet.2012.05.010.
[37] M. Najibah, J. Hnát, M. Plevová, A. Dayan, J. Stojadinovic, J. Žitka, C. Bae, K. Bouzek, D. Henkensmeier, PPS-reinforced poly(terphenylene) anion-exchange membranes with different quaternary ammonium groups for use in water electrolysers, J. Membr. Sci. 713 (2025) 123335, https://doi.org/10.1016/j.memsci.2024.123335.
[38] B. Li, Y. Wu, H. Cheng, W. Liu, Synthesis of linear isotactic-rich poly(p-methylstyrene) via cationic polymerization coinitiated with AlCl3, Polymer 53 (2012) 3726–3734, https://doi.org/10.1016/j.polymer.2012.04.003.
[39] P.A. Neale, A.I. Schäfer, Magnetic ion exchange: is there potential for international development? Desalination 248 (2009) 160–168, https://doi.org/10.1016/j.desal.2008.05.052.
[40] J. Tong, B. Chang, Y. Liu, B. Li, Y. Zhang, L. Han, J. Wang, K. Hu, K. Shi, J. Yang, Efficient capture of ReO4−/TcO4− on anion exchange resin from wastewater, Separ. Purif. Technol. 352 (2025) 128168, https://doi.org/10.1016/j.seppur.2024.128168.
[41] Y. Gu, Y. Sun, Quaternary phosphonium strong based anion exchangers for the selective adsorption of nitrate, Chem. Eng. J. 485 (2024) 149650, https://doi.org/10.1016/j.cej.2024.149650.
[42] S. Wiriyathamcharoen, S. Sarkar, P. Jiemvarangkul, T.T. Nguyen, W. Klysubun, S. Padungthon, Synthesis optimization of hybrid anion exchanger containing triethylamine functional groups and hydrated Fe(III) oxide nanoparticles for simultaneous nitrate and phosphate removal, Chem. Eng. J. 381 (2020) 122671, https://doi.org/10.1016/j.cej.2019.122671.
[43] Y. Gao, W. Wu, L. Shen, J. Qu, Y. Li, D. Sun, Z. Dong, L. Ding, Adsorption behavior and mechanism insight of organoarsenic compounds on magnetic ion exchange resin based on the combined method of DFT calculation and characterization, J. Water Proc. Eng. 70 (2025) 107029, https://doi.org/10.1016/j.jwpe.2025.107029.
[44] G. Duan, X. Li, X. Ma, W. Zhong, S. Wang, High-efficiency adsorption removal for cu(II) and ni(II) using a novel acylamino dihydroxamic acid chelating resin, Sci. Total Environ. 864 (2023) 160984, https://doi.org/10.1016/j.scitotenv.2022.160984.
[45] J. Wang, C. Chen, J.J. Huang, N. Xiao, S. Li, Synchronous or selective removal of nitrate and Cr(VI) by montmorillonite supported sulfidized nanoscale zerovalent iron: role of Fe(II) and S0, Separ. Purif. Technol. 354 (2025) 129006, https://doi.org/10.1016/j.seppur.2024.129006.
[46] S.O. Abayie, T. Leiviskä, Removal of nitrate from underground mine waters using selective ion exchange resins, J. Environ. Chem. Eng. 10 (2022) 108642, https://doi.org/10.1016/j.jece.2022.108642.
[47] S. Han, Y. Zang, Y. Gao, Q. Yue, P. Zhang, W. Kong, B. Jin, X. Xu, B. Gao, Co-monomer polymer anion exchange resin for removing Cr(VI) contaminants: adsorption kinetics, mechanism and performance, Sci. Total Environ. 709 (2020) 136002, https://doi.org/10.1016/j.scitotenv.2019.136002.
[48] T. Hu, W. Hao, H. Zou, W. Xue, D. Mei, Y. Song, W. Yan, Highly selective removal of Technetium-99 using imidazolium-based macroporous anion exchange resins, Chem. Eng. J. 465 (2023) 142951, https://doi.org/10.1016/j.cej.2023.142951.
[49] S. Samatya, N. Kabay, Ü. Yüksel, M. Arda, M. Yüksel, Removal of nitrate from aqueous solution by nitrate selective ion exchange resins, React. Funct. Polym. 66 (2006) 1206–1214, https://doi.org/10.1016/j.reactfunctpolym.2006.03.009.
[50] B. Gu, Y.-K. Ku, P.M. Jardine, Sorption and binary exchange of nitrate, sulfate, and uranium on an anion-exchange resin, Environ. Sci. Technol. 38 (2004) 3184–3188, https://doi.org/10.1021/es034902m.
[51] Y. Zong, X. Wang, H. Zhang, Y. Li, J. Yu, C. Wang, Z. Cai, J. Wei, L. Ding, Preparation of a ternary composite based on water caltrop shell derived biochar and gelatin/alginate for cadmium removal from contaminated water: performances assessment and mechanism insight, Int. J. Biol. Macromol. 234 (2023) 123637, https://doi.org/10.1016/j.ijbiomac.2023.123637.
[52] T.N. Dharmapriya, H.-Y. Shih, P.-J. Huang, Facile synthesis of hydrogel-based ion-exchange resins for nitrite/nitrate removal and studies of adsorption behavior, Polymers 14 (2022) 1442, https://doi.org/10.3390/polym14071442.
[53] X. Xu, B. Gao, Y. Zhao, S. Chen, X. Tan, Q. Yue, J. Lin, Y. Wang, Nitrate removal from aqueous solution by arundo donax L. reed based anion exchange resin, J. Hazard. Mater. 203–204 (2012) 86–92, https://doi.org/10.1016/j.jhazmat.2011.11.094.
[54] J. Pan, B. Gao, W. Song, X. Xu, B. Jin, Q. Yue, Column adsorption and regeneration study of magnetic biopolymer resin for perchlorate removal in presence of nitrate and phosphate, J. Clean. Prod. 213 (2019) 762–775, https://doi.org/10.1016/j.jclepro.2018.12.085.
[55] M. Stjepanović, N. Velić, M. Habuda-Stanić, Modified grape seeds: a promising alternative for nitrate removal from water, Materials 14 (2021) 4791, https://doi.org/10.3390/ma14174791.
[56] S. Rungrodnimitchai, D. Kotatha, New adsorbents for nitrate from modified ground tire rubber, React. Funct. Polym. 136 (2019) 9–18, https://doi.org/10.1016/j.reactfunctpolym.2018.12.011.
[57] B. Zeng, B. Tao, Z. Pan, L. Shen, J. Zhang, H. Lin, A low-cost and sustainable solution for nitrate removal from secondary effluent: macroporous ion exchange resin treatment, J. Environ. Manag. 347 (2023) 119142, https://doi.org/10.1016/j.jenvman.2023.119142.
[58] T. Nur, W.G. Shim, P. Loganathan, S. Vigneswaran, J. Kandasamy, Nitrate removal using purolite A520E ion exchange resin: batch and fixed-bed column adsorption modelling, Int. J. Environ. Sci. Technol. 12 (2015) 1311–1320, https://doi.org/10.1007/s13762-014-0510-6.
[59] Q. Li, X. Lu, C. Shuang, C. Qi, G. Wang, A. Li, H. Song, Preferential adsorption of nitrate with different trialkylamine modified resins and their preliminary investigation for advanced treatment of municipal wastewater, Chemosphere 223 (2019) 39–47, https://doi.org/10.1016/j.chemosphere.2019.02.008.
[60] M. Shen, Y. Liu, Q. Yin, H. Zhang, H. Chen, Enhanced thermal and mass diffusion in maxwell nanofluid: a fractional brownian motion model, Fractal and Fractional 8 (2024) 491, https://doi.org/10.3390/fractalfract8080491.
[61] H. Loulijat, H. Moustabchir, Numerical study of the effects of brownian motion and interfacial layer on the viscosity of nanofluid (au-H2O), J. Mol. Liq. 350 (2022) 118221, https://doi.org/10.1016/j.molliq.2021.118221.
[62] Q. Yuan, Y. Duan, L. Fan, C. Zheng, R. Su, N. Liu, J. Wu, Efficient adsorption and mechanistic analysis of phosphorus in acid leaching solution of incinerated sewage sludge ash by zirconium-modified reed biochar, Separ. Purif. Technol. 359 (2025) 130535, https://doi.org/10.1016/j.seppur.2024.130535.
[63] B. Wang, Y. Zhai, T. Hu, Q. Niu, S. Li, X. Liu, X. Liu, Z. Wang, C. Li, M. Xu, Green quaternary ammonium nitrogen functionalized mesoporous biochar for sustainable electro-adsorption of perchlorate, Chem. Eng. J. 419 (2021) 129585, https://doi.org/10.1016/j.cej.2021.129585.
[64] J. Tong, J. Yang, X. Li, K. Hu, Y. Lu, M. Wang, Y. Hu, K. Shi, Ultrafast and selective capture of 99TcO4-/ReO4- from wastewater by hyper-branched quaternary ammonium group-functionalized resin, J. Hazard Mater. 466 (2024) 133671, https://doi.org/10.1016/j.jhazmat.2024.133671.
[65] M.M. Salehi, S.M. Nezhad, L. Choopani, S. Asghari, S.M. Safavi, F. Shirini, H. Gholamikafshgari, A. Maleki, E.N. Zare, Magnetic carrageenan gum-grafted-polyacrylamide nanocomposite for uptake of cationic dyes from the aquatic systems, Int. J. Biol. Macromol. 283 (2024) 137796, https://doi.org/10.1016/j.ijbiomac.2024.137796.
[66] P.-H. Chang, Y. Yang, Y. Wen, M.M.M. Ahmed, J.-C. Chang, T.-Y. Chang, Y.-M. Tzou, Z. Li, A.I. Osman, Efficient ethidium bromide removal using sodium alginate/graphene oxide composite beads: insights into adsorption mechanisms and performance, Chem. Eng. J. 500 (2024) 156379, https://doi.org/10.1016/j.cej.2024.156379.
[67] H.A.T. Banu, P. Karthikeyan, S. Vigneshwaran, S. Meenakshi, Adsorptive performance of lanthanum encapsulated biopolymer chitosan-kaolin clay hybrid composite for the recovery of nitrate and phosphate from water, Int. J. Biol. Macromol. (2020), https://doi.org/10.1016/j.ijbiomac.2020.03.074.
[68] J. Pan, B. Gao, W. Song, X. Xu, Q. Yue, Modified biogas residues as an eco-friendly and easily-recoverable biosorbent for nitrate and phosphate removals from surface water, J. Hazard Mater. 382 (2020) 121073, https://doi.org/10.1016/j.jhazmat.2019.121073.
[69] Y. Hu, J. Foster, T.H. Boyer, Selectivity of bicarbonate-form anion exchange for drinking water contaminants: influence of resin properties, Separ. Purif. Technol. 163 (2016) 128–139, https://doi.org/10.1016/j.seppur.2016.02.030.
[70] L. Li, Y. Liu, Adsorption of perchlorate on different quaternary ammonium-modified resins: influencing factors and mechanisms, Separ. Purif. Technol. 358 (2025) 130364, https://doi.org/10.1016/j.seppur.2024.130364.

[71] Y. Tang, Q. Wen, Z. Chen, Simultaneous removal of nitrogen and phosphorus nutrients from secondary effluent by magnetic resin containing two types of quaternary ammonium adsorption sites: preparation, characterization, and application, Chem. Eng. J. 477 (2023) 147137, https://doi.org/10.1016/j.cej.2023.147137.

[72] T. Wang, J. Fu, X. Gao, G. Li, D. Liu, Pore engineering of MOF-808 for effective adsorption of roxarsone, Separ. Purif. Technol. 348 (2024) 127724, https://doi.org/10.1016/j.seppur.2024.127724.

[73] Y. Li, M. Wu, J. Wu, Y. Wang, Z. Zheng, Z. Jiang, Mechanistic insight and rapid co-adsorption of nitrogen pollution from micro-polluted water over MgAl-layered double hydroxide composite based on zeolite, Separ. Purif. Technol. 297 (2022) 121484, https://doi.org/10.1016/j.seppur.2022.121484.